

Automated determination of g-mode period spacing of red-giant stars

Abhisek Datta¹, Anwesh Mazumdar², Umang Gupta³, and Saskia Hekker^{4,5,6}

¹*Department of Physics, Indian Institute of Technology Kharagpur, Kharagpur 721302, India.*

²*Homi Bhabha Centre for Science Education, TIFR, V. N. Purav Marg, Mankhurd, Mumbai 400088, India.*

³*Department of Electrical Engineering, Indian Institute of Technology Delhi, Hauz Khas, New Delhi 110016, India.*

⁴*Astronomical Institute ‘Anton Pannekoek’, University of Amsterdam, Science Park 904, 1098 HX Amsterdam, the Netherlands.*

⁵*Max Planck Institut für Sonnensystemforschung, Justus-von-Liebig-Weg 3, 37077 Göttingen, Germany.*

⁶*Stellar Astrophysics Centre, Department of Physics and Astronomy, Aarhus University, Ny Munkegade 120, DK-8000 Aarhus C, Denmark.*

3 December 2014

ABSTRACT

The *Kepler* satellite has provided photometric timeseries data of unprecedented length, duty cycle and precision. To fully analyse these data for the tens of thousands of stars observed by *Kepler*, automated methods are a prerequisite. Here we present an automated procedure to determine the period spacing of gravity modes in red-giant stars ascending the red-giant branch. The gravity modes reside in a cavity in the deep interior of the stars and provide information on the conditions in the stellar core. However, for red giants the gravity modes are not directly observable on the surface, hence this method is based on the pressure-gravity mixed modes that present observable features in the Fourier power spectrum. The method presented here is based on the vertical alignment and symmetry of these mixed modes in a period echelle diagram. We find that we can obtain reliable results for both model frequencies and observed frequencies. Additionally, we carried out Monte Carlo tests to obtain realistic uncertainties on the period spacings with different set of oscillation modes (for the models) and uncertainties on the frequencies. Furthermore, this method has been used to improve mode detection and identification of the observed frequencies in an iterative manner.

1 INTRODUCTION

Red giants are evolved stars which have a hydrogen-depleted core surrounded by a hydrogen-burning shell. Further evolved red giants also burn helium in their core. Although the structure of red giants is broadly understood from the theory of stellar structure and evolution, several important questions remain, such as the mechanism of convective heat flow, nuclear processes in extremely dense material, and transport of angular momentum through differential rotation. Several recent studies have indeed focussed on these questions using the techniques of asteroseismology which is the study of stellar oscillation frequencies.

Among the recent results obtained are the detection of signatures from the core through so-called mixed oscillation modes (Beck et al. 2011; Bedding et al. 2011; Mosser et al. 2012a, 2014) and theoretical explanations of these modes (Christensen-Dalsgaard 2008; Dupret et al. 2009; Montalbán et al. 2010; Christensen-Dalsgaard 2011). These mixed modes are subsequently used to probe differential rotation in the stars (Beck et al. 2012; Deheuvels et al. 2012; Mosser et al. 2012b; Deheuvels et al. 2014). Efforts to fully incorporate rotation and angular momentum transport in

stellar evolution models have been made, but these results do not yet provide results consistent with observations (Ceillier et al. 2013; Goupil et al. 2013; Marques et al. 2013; Ouazzani et al. 2013; Goupil et al. 2014; Cantiello et al. 2014).

In general, there are two main sets of solutions for the equation of motion of a pulsating star and these lead to two types of pulsation modes: p-modes and g-modes (for a detailed discussion on these, see Chaplin & Miglio (2013) and Hekker (2013)). Due to the large density gradient outside the helium core, a red giant is effectively divided into two cavities. In the envelope, the non-radial oscillations behave as p-modes, while in the core they behave like g-modes. The models predict a very dense spectrum of these so-called mixed modes for each value of l (except $l = 0$). Details about mixed modes and resonant coupling between the two cavities in red giants have been described by Bedding et al. (2011) and Hekker & Mazumdar (2014). The resonant coupling causes some of the mixed modes to have a high amplitude in the envelope and these are called p-dominated mixed modes. Theoretically, the oscillation modes in red giants can be characterised by the dimensionless mode inertia,

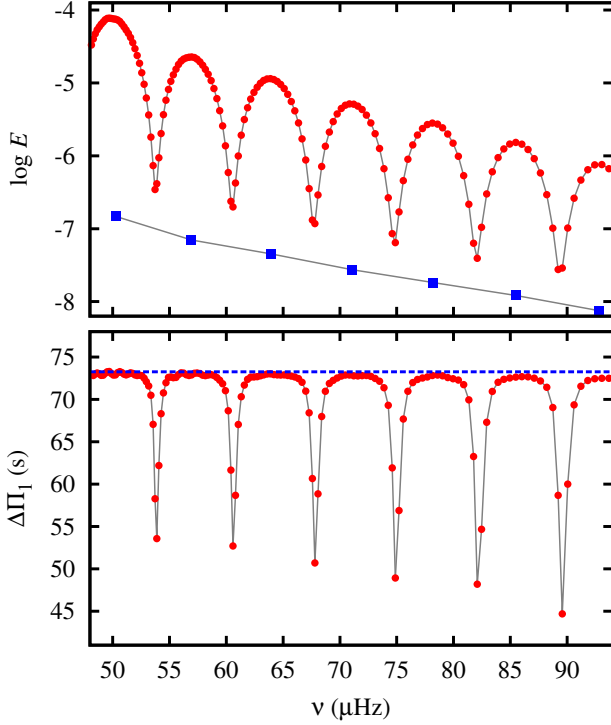


Figure 1. Mode inertia and period spacing of a $1M_{\odot}$ red-giant model at an age of 12.5 Gyr (Model 2 in Fig. 7) are plotted as functions of frequency for $l = 0$ modes (blue squares) and $l = 1$ modes (red dots). The top panel shows the mode inertia, while the bottom panel shows the period spacing. The horizontal dashed blue line indicates the asymptotic value of the dipole modes, $\Delta\Pi_{1,g}$ ($= 73.48$ s), as determined from Eq. (1) using the model.

E , which is a measure of the energy in the mode (see, e.g., Aerts et al. 2010). The non-radial modes, in general, have much higher inertia compared to the radial ones, except for the few p-dominated mixed modes in each radial order which possess inertia of the same order of magnitude as the radial modes. This is shown in Fig. 1 for a $1M_{\odot}$ red-giant model at an age of 12.5 Gyr in the shell hydrogen-burning phase (Model 2 in Fig. 7). The details of the model can be found in Section 3.1. For the sake of clarity, we show only the radial ($l = 0$) and dipole ($l = 1$) modes in this figure; the higher degree non-radial modes ($l > 1$) will have similar behaviour as the dipole modes, though the exact distribution of mode inertia depends on the evolutionary state of the star. The modes with the highest inertia in each radial order are the g-dominated ones, with very little amplitude in the p-mode cavity. Observationally, only the modes with low inertia attain significant heights in the power spectrum and can be detected (Dupret et al. 2009).

The g-modes are approximately equi-spaced in period (denoted by Π) with an asymptotic value of the period spacing, $\Delta\Pi_{l,g}$, being given by

$$\Delta\Pi_{l,g} = \frac{\Pi_0}{\sqrt{l(l+1)}}(n_g + \epsilon_g), \quad (1)$$

where

$$\Pi_0 = 2\pi^2 \left(\int_g \frac{N}{r} dr \right)^{-1}, \quad (2)$$

N being the Brunt-Väisälä frequency. The integral is carried out over the g-mode cavity. This equal spacing in period holds for the underlying pure g-modes in the core, as referred to as γ modes by Aizenman et al. (1977); Bedding (2014). In reality, this period spacing would be found in the most g-dominated modes (at the inertia maxima in the top panel of Fig. 1), while the modes with p-dominated character will have a smaller spacing in period. This is illustrated in the bottom panel of Fig. 1, where the dips in the period spacing correspond to the minima in the inertia, while the g-dominated modes maintain a period spacing very close to the asymptotic value given in Eq. (1).

In Fig. 2(a), the frequencies with azimuthal order $m = 0$ of a $1M_{\odot}$ red giant model at an age of 12.6 Gyr (Model 3 in Fig. 7) are plotted as a function of the period spacing $\Delta\Pi_1$. The vertical ridge in this figure represents the value of the g-mode period spacing, $\Delta\Pi_{1,g}$, while the p-dominated modes have much smaller values of $\Delta\Pi_1$. We do not expect a $\Delta\Pi_{1,g}$ value higher than the asymptotic one, and the only case where one can find such a value in the observations is when one or more intermediate non-radial modes have not been detected between two observed peaks in the power spectrum.

If the frequencies of the $l = 1$ modes are plotted as a function of Π_1 modulo $\Delta\Pi_{1,g}$ (Π_1 being the period of $l = 1$ modes), one can expect a vertical alignment of the $l = 1$ modes with the same azimuthal order (see, e.g., Bedding et al. 2011). Such a diagram, known as the period echelle diagram, is shown in Fig. 2(b) for the same stellar model as in Fig. 2(a). The almost vertically aligned modes in this diagram are the g-dominated dipole modes. The modes placed away from this vertical ridge are more mixed in character, with the most extremely deviant ones being the most p-dominated modes. At low frequencies the ridge becomes curved as a result of the difference between the period spacing obtained asymptotically and from individual frequencies in the observable frequency range.

The g-mode period spacing of red giants can be used to distinguish between their evolutionary phases, i.e., shell hydrogen-burning and core helium-burning, as shown by Bedding et al. (2011). In their work the vertical stacking in the period echelle diagram was shown to give the g-mode period spacing, although no quantitative formulation to determine $\Delta\Pi_{1,g}$ was given. In the present work we describe an automated technique to determine the g-mode period spacing by recognising the vertical stacking of the g-dominated modes and the roughly symmetrical deviation of the p-dominated modes from this vertical ridge in the period echelle diagram.

The asymptotic value of the g-mode period spacing, obtained from Eq. (1), is usually slightly higher than the actual value obtained from the frequencies of the model. For the particular model shown in Fig. 2, for example, the asymptotic value of $\Delta\Pi_{1,g}$ is 62.15 s, while the value obtained from the frequencies is 62.05 s. This slight difference is a reflection of the validity of the asymptotic treatment. In any case, this difference is much smaller than the uncertainty in $\Delta\Pi_{1,g}$ that would be introduced by the random uncertainties in the measurement of the stellar frequencies. Thus, an estimate of $\Delta\Pi_{1,g}$ from observed frequencies can be considered as a reliable approximation to its asymptotic form as given by Eq. (1).

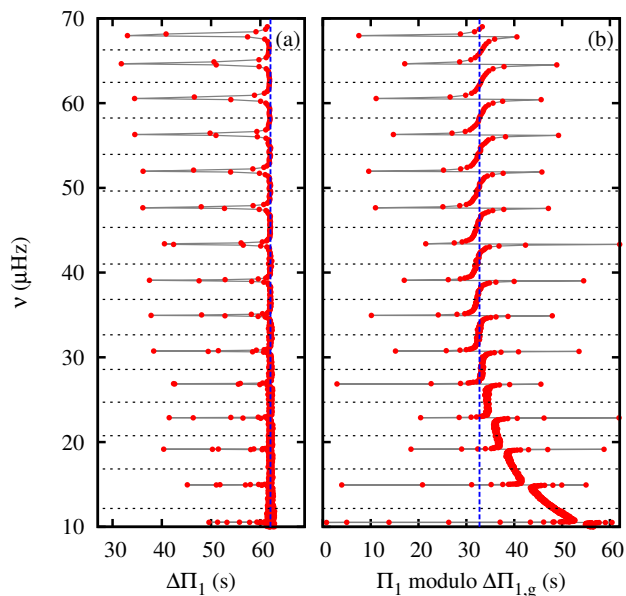


Figure 2. (a) Frequency vs period spacing for $l = 1$ modes for a $1M_{\odot}$ red-giant model at an age of 12.6 Gyr (Model 3 in Fig. 7). The blue dashed line shows the g-mode period spacing of high order g-modes. (b) Period echelle diagram for the $l = 1$ modes of the model with $\Delta\Pi_{1,g} = 62.05$ s. The blue dashed line indicates the vertical alignment of the high-order g-dominated modes. In both panels the red points connected with the light grey lines are $l = 1$ modes and the horizontal dotted lines represent the frequencies of the radial modes.

2 G-MODE PERIOD SPACING FINDER (GPS)

The period echelle diagram for red giants, using only oscillations with $m = 0$ as shown in Fig. 2(b), has two important features, namely, vertical alignment of the g-dominated modes and the roughly symmetrical deviation of the p-dominated modes from this vertical ridge. The inertias of the g-dominated modes are much higher and their amplitudes and heights in the observed power spectrum are correspondingly lower (Dupret et al. 2009). This means that only modes with lower inertias, i.e., modes with sufficient amplitude in the p-mode region can be observed in the actual data even with the best available instruments like *Kepler*. The period spacing of these observed p-modes ($\Delta\Pi_l$) is much smaller than those of the g-dominated modes ($\Delta\Pi_{l,g}$). However, it is $\Delta\Pi_{l,g}$ which has diagnostic power to probe the innermost layers of the star through the asymptotic relation discussed above. Therefore, a method to determine $\Delta\Pi_{l,g}$ from $\Delta\Pi_l$ is of considerable interest. For $l = 2$ and $l = 3$, only the most p-dominated modes are usually visible, if at all, which makes it difficult to draw any inference about the period spacing. For $l = 1$, however, several mixed modes can be detected around the most p-dominated modes. Even though the period spacing of these modes is far different from the period spacing of the g-dominated modes, they contain information about the deep interior through the coupling between the outer and inner oscillation cavities. It turns out that it is possible to exploit the underlying vertical alignment pattern of the period echelle diagram to estimate $\Delta\Pi_{1,g}$ reliably from these p-dominated mixed $l = 1$ modes. Indeed, the g-mode period

spacing for a few red giants was determined by Bedding et al. (2011) by demanding such a vertical alignment in the period echelle diagram. However, they do not provide any standard prescription to determine $\Delta\Pi_{1,g}$ from an observed set of frequencies.

Mosser et al. (2012a) further developed this using an empirical approach to find p- and g-dominated mixed dipole modes combined with an asymptotic development to obtain the asymptotic period spacing based on work by Shibahashi (1979) and Unno et al. (1989). This development is based on the fact that eigenfrequencies are derived from an implicit equation relating the coupling of the p and g waves:

$$\tan \theta_p = q \tan \theta_g, \quad (3)$$

where θ_p and θ_g are the p- and g-wave phases. The dimensionless coefficient q indicates the level of mixing (Mosser et al. 2012a). This was then used to derive an expression for dipole mixed modes coupled to a pure pressure dipole mode ($\nu_{n_p, l=1}$):

$$\nu = \nu_{n_p, l=1} + \frac{\Delta\nu}{\pi} \arctan(q \tan \pi((\Delta\Pi_1 \nu)^{-1} - \epsilon_g)), \quad (4)$$

where ϵ_g is a phase term (Mosser et al. 2012a). Eq. (4) is essentially the mathematical expression of the tangential shape of the mixed dipole modes in each p-mode order, in which the coupling q is connected to the steepness of the “S”-shape and ϵ_g represents an offset.

In the work presented here, we construct an algorithm to find $\Delta\Pi_{1,g}$ in a systematic search method that achieves the vertical stacked pattern in the period-echelle diagram as indicated by Bedding et al. (2011). This algorithm is called ‘GPS’. GPS has been tested on both stellar models as well as actual observed frequencies of red-giant stars observed with the *Kepler* satellite. The algorithm is described in detail in the next subsection. Although we do not use the function derived by Mosser et al. (2012a) (Eq. (4)) in GPS, we have performed tests to verify our results with such fits. In all cases we obtain consistent results.

2.1 Algorithm

As can be seen from Fig. 2, the $l = 0$ and $l = 1$ frequencies of a red giant, if arranged in increasing order of frequencies, appear as a dense spectrum of the dipole modes with a few radial modes separating them at regular intervals. This feature is used by GPS to separate the entire range of $l = 1$ modes into sets referred to as “bands”. A band is a set of $l = 1$ modes lying between two consecutive $l = 0$ modes, i.e., one p-mode order. The horizontal dashed lines in Fig. 2 are the boundaries of the bands. For observed spectra, of course, the number of dipole modes in a band is much less than that for a model.

The g-dominated dipole modes of high order are equally spaced in period. Thus for a correct choice of the period spacing $\Delta\Pi_{1,g}$ to construct the period echelle diagram, these g-dominated $l = 1$ modes in a band would align to form a nearly vertical central ridge. Since each band is bordered by two radial modes, the presence of an underlying $l = 1$ p-mode is expected around the middle of the band. This mode would give rise to a few p-dominated mixed modes which would be farthest from the central vertical ridge of the band. In moving from one radial mode to the next, a

horizontal “wrap around” is thus expected in the period echelle diagram. The presence of such a shift from the extreme right to the extreme left is considered as a necessary condition for a band to be considered for vertical alignment.

Usually the mixed p-dominated modes are expected in a short frequency range centred around the underlying $l = 1$ p-mode. This would imply that these modes would be approximately at equal distances from the central ridge in the period echelle diagram, creating symmetrical upper and lower tails of the ridge, i.e., this symmetry reflects an implicit assumption of $\epsilon_g \sim 0.5$. However, this symmetry is not perfect as the frequencies of the mixed modes would depend on the exact frequencies of the underlying pure p- and g-modes as well as the extent of mixing on either side of the central mode.

Therefore, ideally at the correct value of $\Delta\Pi_{1,g}$ in the period echelle diagram, all the bands should align vertically to form the central ridge with the mixed p-dominated modes forming roughly symmetrical tails on either side. Since the g-dominated modes also have mixed character, the central ridge in the bands are not perfectly vertical but form a “S-shaped” structure with long tails as seen in Fig. 2. The aim is to obtain this alignment pattern in the period echelle diagram by scanning through possible values of $\Delta\Pi_{1,g}$ and choosing the correct value which achieves such a pattern.

The algorithm implemented by GPS consists of the following steps to arrive at the correct g-mode period spacing value. The abscissa of the period echelle diagram is henceforth denoted by $\Pi_r \equiv \Pi_1 \bmod \Delta\Pi_{1,g} \equiv \Pi_1 \% \Delta\Pi_{1,g}$.

(i) *Lower frequency threshold*: The asymptotic period spacing given by Eq. (1) is valid only for high order g-modes. At low frequencies, the modes have even higher orders compared to the modes that are in the observable frequency range and hence would give a period spacing based on individual frequencies closer to the asymptotic value. As only modes in the observable frequency range are considered here, the difference between the period spacing obtained from individual frequencies and the asymptotic value is manifested as a curvature in the period echelle diagram, as seen in Fig. 2. To account for this a lower threshold on frequency is necessary before GPS can be applied. However, it is difficult to arrive at a specific threshold frequency in an analytic fashion. Different criteria for the lower threshold were tried for a large number of models spanning the entire red-giant branch (RGB) and the following prescription was adopted heuristically:

$$\nu_{\text{threshold}} = \begin{cases} 7.5 \mu\text{Hz}, & \text{for } \nu_{\text{max}} < 15 \mu\text{Hz} \\ 0.5 \nu_{\text{max}}, & \text{for } 15 \mu\text{Hz} \leq \nu_{\text{max}} \leq 160 \mu\text{Hz} \\ 80 \mu\text{Hz}, & \text{for } \nu_{\text{max}} > 160 \mu\text{Hz} \end{cases} \quad (5)$$

Successful tests with several observed stars confirmed this choice.

(ii) *Band Identification*: In the period echelle diagram, a band refers to the $l = 1$ modes (points in Fig. 2) lying between two successive $l = 0$ modes (dotted lines in the same figure). The bands are indexed starting from the lowest frequencies to the highest ones. For a band to be considered for the vertical alignment, it has to satisfy two conditions. First, the Π_r for the highest frequency of a band must be less than that for the lowest frequency of the band immediately above, i.e., the Π_r value increases from the top end of one band to

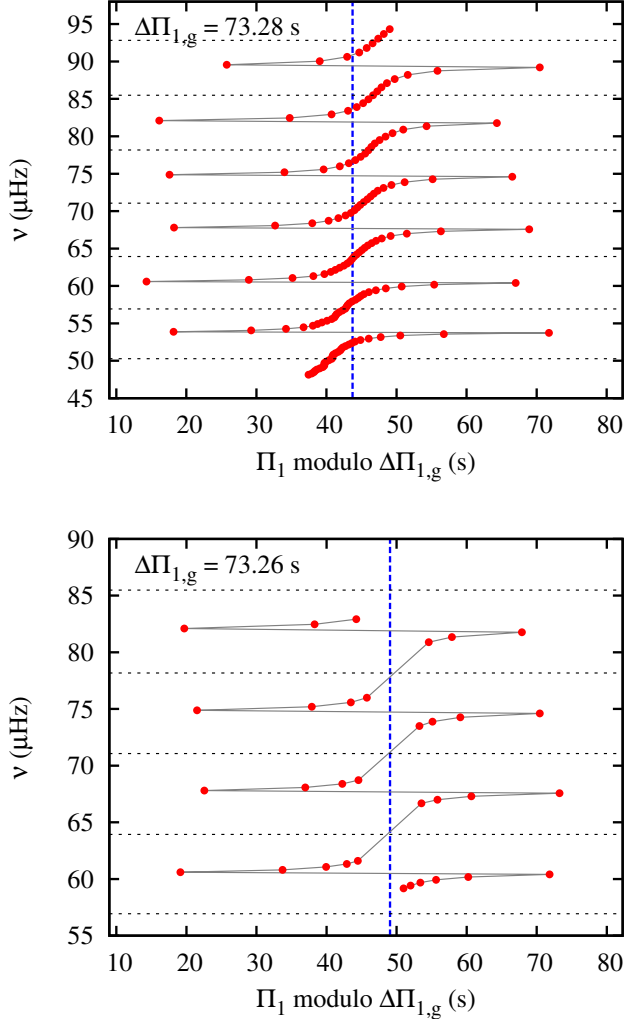


Figure 3. Two period echelle diagrams with different density of $l = 1$ modes for a $1M_{\odot}$ red-giant model are shown. The symbols and the lines have the same meaning as in Fig. 2. The top panel shows the period echelle diagram for all the $l = 1$ modes in a frequency range spanning 7 radial orders, with $\Delta\Pi_{1,g} = 73.28$ s as determined by GPS. The lower panel shows the period echelle diagram for only a subset of the most p-dominated $l = 1$ modes in a smaller frequency range consisting of 5 radial orders with $\Delta\Pi_{1,g} = 73.26$ s. To illustrate the symmetrical distribution of the most p-dominated modes, the abscissae have been offset slightly in both diagrams.

the bottom end of the next band. Second, one and only one nearly horizontal shift between the two most p-dominated modes in a band, i.e., from the extreme right to the extreme left of the period echelle diagram should be present. Any band which does not satisfy these two conditions is not used in the vertical alignment in the period echelle diagram. GPS proceeds to the next step only if the number of bands which do not satisfy these conditions is less than or equal to two.

(iii) *Vertical Alignment*: This step quantifies the vertical stacking of the central g-dominated $l = 1$ modes in the period echelle diagram for a given trial value of $\Delta\Pi_{1,g}$. This is done by first estimating the position of the most g-dominated mode at the upper boundary of each band in

the period echelle diagram and then calculating the dispersion of these positions for all bands from an average vertical ridge. This dispersion would later be minimised to obtain the correct value of $\Delta\Pi_{1,g}$.

The location of the most g-dominated mode at the upper boundary of each band is estimated as follows. At the upper boundary of a band (say, the i^{th} band), the weighted average value of Π_r of the highest dipole mode in that band (denoted by the index (i, h)) and the lowest dipole mode in the next band (denoted by the index $(i+1, l)$) is calculated. These two $l = 1$ modes are the immediate neighbours of the radial mode separating the i^{th} and the $(i+1)^{\text{th}}$ bands (denoted by $\nu_{l=0}^{(i,i+1)}$). For observed frequencies, the differences in frequency between each of these $l = 1$ modes and the radial mode between them can be significant and may not even have similar values. To account for this difference in frequency we incorporate a weighing. The weights are taken as the differences in frequency between the respective $l = 1$ mode and the neighbouring $l = 0$ mode. The weighted mean thus calculated is an estimate of the Π_r value of the (possibly unseen) most g-dominated mode at the boundary of the two bands. It is denoted by $\Pi_r^{(g,i)}$ for the i^{th} band and is calculated as follows:

$$\Pi_r^{(g,i)} = \frac{y^{(i)}\Pi_r^{(i+1,l)} + y^{(i+1)}\Pi_r^{(i,h)}}{y^{(i+1)} + y^{(i)}} \quad (6)$$

where $y^{(i+1)} = \nu_{l=1}^{(i+1,l)} - \nu_{l=0}^{(i,i+1)}$ and $y^{(i)} = \nu_{l=0}^{(i,i+1)} - \nu_{l=1}^{(i,h)}$.

From all the values of $\Pi_r^{(g,i)}$ calculated for each accepted band, their arithmetic mean, $\Pi_r^{(g)}$, is determined which is called the average midpoint, for a particular choice of $\Delta\Pi_{1,g}$. This is considered as the mean position of the central vertical ridge. The squared deviation χ_{vert}^2 of the $\Pi_r^{(g,i)}$ values for each accepted band from this mean position is calculated as

$$\chi_{\text{vert}}^2 = \sum_{i=1}^N \frac{(\Pi_r^{(g,i)} - \Pi_r^{(g)})^2}{(\delta\Pi_r^{(g,i)})^2} \quad (7)$$

where $\delta\Pi_r^{(g,i)} = \frac{1}{2}\sqrt{(\delta\Pi_r^{(i+1,l)})^2 + (\delta\Pi_r^{(i,h)})^2}$ is the uncertainty in $\Pi_r^{(g,i)}$ and the total number of accepted bands is N . Here, $\delta\Pi_r^{(i+1,l)} = \delta\nu_{l=1}^{(i+1,l)}/(\nu_{l=1}^{(i+1,l)})^2$ and $\delta\Pi_r^{(i,h)} = \delta\nu_{l=1}^{(i,h)}/(\nu_{l=1}^{(i,h)})^2$, where $\delta\nu$ refers to the uncertainty in the observed frequencies. We have not considered the uncertainties in the weighing factors $y^{(i)}$ and $y^{(i+1)}$.

Among all trial values of $\Delta\Pi_{1,g}$, higher priorities are given to the cases with lesser number of unacceptable bands. Minimisation of χ_{vert}^2 alone among the cases with lowest number of unacceptable bands would give the best vertical alignment of the bands. In Fig. 3, in both period echelle diagrams, there are no unacceptable bands and a vertical alignment has been achieved.

(iv) *Symmetrical distribution*: As described before, besides the vertical alignment of the g-dominated modes to form the central ridge, a nearly symmetrical distribution of the p-dominated modes is also expected around the central ridge in the period echelle diagram, i.e., $\epsilon_g \sim 0.5$. This symmetrical positioning of the tails on either side can be seen in both the period echelle diagrams in Fig. 3. This criterion is implemented in GPS in the following way. The arithmetic mean of the two extreme p-dominated mode frequencies on

either side of the central ridge in the i^{th} band is

$$\Pi_r^{(p,i)} = \frac{\Pi_r^{(i,r)} + \Pi_r^{(i,l)}}{2}, \quad (8)$$

where $\Pi_r^{(i,r)}$ and $\Pi_r^{(i,l)}$ refer to the $l = 1$ mode frequencies located on the extreme right ($\nu_{l=1}^{(i,r)}$) and left ($\nu_{l=1}^{(i,l)}$) of the period echelle diagram in the i^{th} band respectively. These are the frequencies between which the “wrap-around” mentioned earlier occurs in the i^{th} band. For a correct choice of $\Delta\Pi_{1,g}$ these modes should be the most p-dominated modes in the i^{th} band, lying on either side of the underlying pure $l = 1$ p-mode. The Π_r value of this underlying pure p-mode would be close to either 0 or $\Delta\Pi_{1,g}$ on the period echelle diagram, that is, it would be farthest removed from the pure g-modes which constitute the central ridge. Therefore, the two most p-dominated modes would be at the two extreme ends of the period echelle diagram and the average of their Π_r values, $\Pi_r^{(p,i)}$, should be close to the central ridge, $\Pi_r^{(g)}$. On the other hand, for a wrong choice of $\Delta\Pi_{1,g}$ both these modes would be on the same side of the period echelle diagram and the value of $\Pi_r^{(p,i)}$ would be far removed from $\Pi_r^{(g)}$; this would indicate an asymmetrical distribution.

The squared deviation of the $\Pi_r^{(p,i)}$ values from the central vertical ridge, $\Pi_r^{(g)}$ (determined in the previous step) is calculated as

$$\chi_{\text{symm}}^2 = \sum_{i=1}^N \frac{(\Pi_r^{(p,i)} - \Pi_r^{(g)})^2}{(\delta\Pi_r^{(p,i)})^2} \quad (9)$$

where $\delta\Pi_r^{(p,i)} = \frac{1}{2}\sqrt{(\delta\Pi_r^{(i,r)})^2 + (\delta\Pi_r^{(i,l)})^2}$. Here, $\delta\Pi_r^{(i,r)} = \frac{\delta\nu_{l=1}^{(i,r)}}{(\nu_{l=1}^{(i,r)})^2}$ and $\delta\Pi_r^{(i,l)} = \frac{\delta\nu_{l=1}^{(i,l)}}{(\nu_{l=1}^{(i,l)})^2}$.

Minimising χ_{symm}^2 alone in the same way as the minimisation of χ_{vert}^2 gives the best possible symmetrical distribution around the central ridge in the period echelle diagram which can be seen in Fig. 3.

(v) *Final minimisation*: To obtain the g-mode period spacing, we minimise the total χ_{tot}^2 which has contributions from both *Vertical Alignment* and *Symmetrical Distribution* in a weighted manner:

$$\chi_{\text{tot}}^2 = (1-a)\chi_{\text{vert}}^2 + a\chi_{\text{symm}}^2 \quad (10)$$

where a is a weighting factor reflecting the emphasis on the *Symmetrical distribution*. It was found that a fixed value of a is not suitable for all stars and it has to be varied over the RGB to get a sensible estimate of $\Delta\Pi_{1,g}$. The idea of symmetrical distribution rests crucially on the assumption that there are two p-dominated modes with very low inertia lying midway between two radial modes. This turns out to be the case in the lower RGB, but not necessarily higher on the RGB. It was found that in the upper RGB a has to be very small. In the lower RGB a is restricted to 0.5 so that equal weightage is given to *Vertical Alignment* and *Symmetrical Distribution*. Different values of a were tried for a large number of models spanning the entire RGB and the following working relation for a was found heuristically.

$$\begin{aligned} a &= 0.0 & \text{for } \Delta\nu < 1.65 \mu\text{Hz} \\ \log a &= A\Delta\nu + B & \text{for } 1.65 \mu\text{Hz} \leq \Delta\nu \leq 12.50 \mu\text{Hz} \\ a &= 0.5 & \text{for } \Delta\nu > 12.50 \mu\text{Hz} \end{aligned} \quad (11)$$

Here A and B are constants which can be determined to

be $A = 0.1566 \mu\text{Hz}^{-1}$ and $B = -2.2584$ from the heuristic exercise. Such a choice of a was found to be appropriate for several observed stars as well.

As mentioned earlier, highest priority is given to the cases with least number of unacceptable bands. Thus the final value of $\Delta\Pi_{1,g}$ is the one which minimises χ_{tot}^2 among all the cases with least number of unacceptable bands.

In the remainder of the paper we show the application of GPS on red-giant models, as well as observed stars, to successfully determine their g-mode period spacing $\Delta\Pi_{1,g}$ along with estimates of uncertainties in the results.

3 APPLICATION OF GPS

3.1 Finding $\Delta\Pi_{1,g}$ of models with GPS

Since the full model frequency spectrum includes the g-dominated modes, the determination of $\Delta\Pi_{1,g}$ is much more straightforward than in observed spectra. In fact, these modes influence the vertical alignment procedure very strongly, while the p-dominated modes play a dominant role in the symmetrical distribution. To illustrate the procedure of GPS a $1 M_{\odot}$ red giant is considered using all the calculated eigenfrequencies.

All the models considered in this work have been constructed using the MESA stellar evolution code (Paxton et al. 2011, version 4798). The models used standard physics such as the OPAL equation of state (Rogers & Nayfonov 2002), OPAL high temperature opacities (Iglesias & Rogers 1996) supplemented by the low temperature opacities from Ferguson et al. (2005). The nuclear reaction rates were from NACRE (Angulo et al. 1999) for all reactions except $^{14}\text{N}(p,\gamma)^{15}\text{O}$ and $^{12}\text{C}(\alpha,\gamma)^{16}\text{O}$, for which updated rates of reaction from Imbriani et al. (2005) and Kunz et al. (2002) were used. Convection was modelled using the standard mixing length theory (Cox & Giuli 1968). Diffusion of helium and heavy elements was not included in the models. We used the standard solar mixture of Grevesse & Sauval (1998). Adiabatic pulsation frequencies of the models were computed with the ADIPLS code (Christensen-Dalsgaard 2008).

Fig. 4 shows the step-by-step procedure followed by GPS. In each of the four parts, the period echelle diagram along with the total χ^2 (χ_{tot}^2) is plotted as $\Delta\Pi_{1,g}$ is varied continuously through trial values. In part (a) of the figure, the trial $\Delta\Pi_{1,g}$ is less than the correct value. Although a number of bands are symmetrically distributed, they are not vertically aligned. In (b) the trial $\Delta\Pi_{1,g}$ is very close to the correct value so that vertical alignment and symmetrical distribution are simultaneously achieved. The trial $\Delta\Pi_{1,g}$ in (c) is slightly greater than the correct value so that the bands are nearly vertically aligned but not symmetrically distributed. In part (d) the trial $\Delta\Pi_{1,g}$ is much greater than the correct value, and thus the bands are neither vertically aligned nor symmetrically distributed. Further, at this value one of the bands is unacceptable because there are more than one shift from the extreme right to the extreme left. The departure of the trial value from the correct value is reflected both in the high χ_{tot}^2 value and the indication of the number of unacceptable bands. The best symmetrical vertical alignment is obtained when χ_{tot}^2 passes through a global minimum, as shown in Fig. 4. The $\Delta\Pi_{1,g}$ for this model is

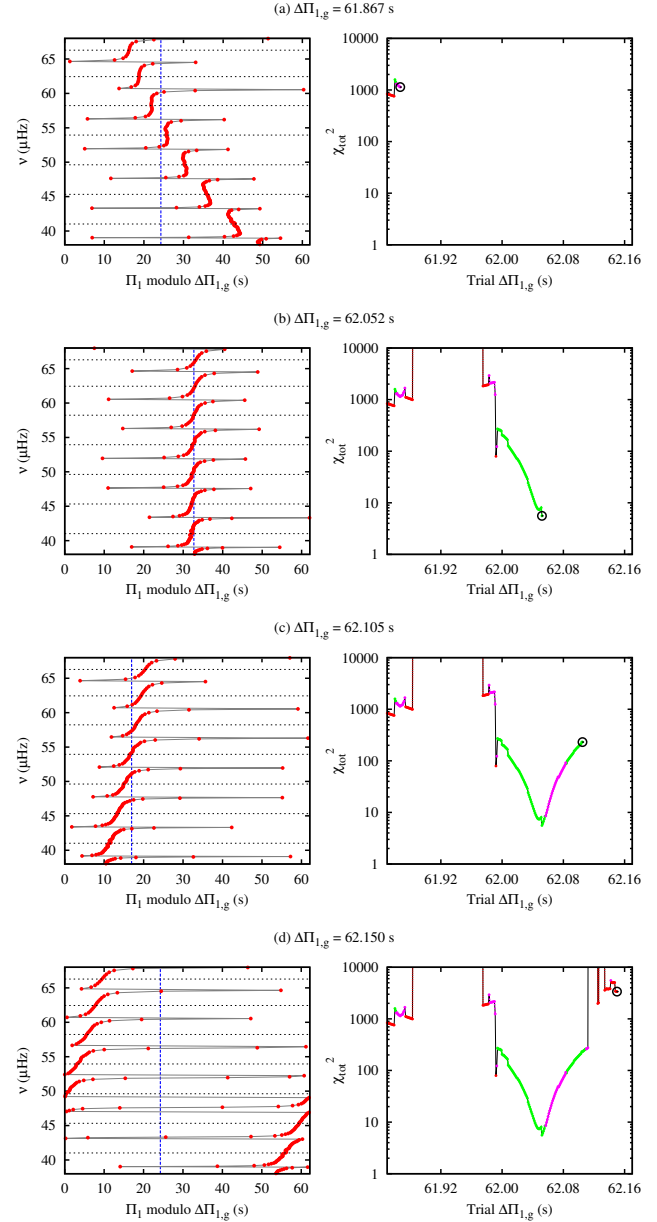


Figure 4. Four snapshots illustrating the method of GPS are shown. Trial values of $\Delta\Pi_{1,g}$ are in increasing order from (a) to (d). In each part, the left panel shows the period echelle diagram, where symbols have the same meaning as in Fig. 2. The right panel shows χ_{tot}^2 as a function of the trial value of $\Delta\Pi_{1,g}$. The trial value used in the left panel corresponds to the last (encircled) point in the corresponding right panel and is indicated at the top of each pair of panels. The colours of the points in the right panel indicate the number of unacceptable bands (red for 2 or more, magenta for 1 and green for 0).

found to be 62.052 s by GPS, which agrees quite well with the asymptotic value of 62.149 s calculated using Eq. (1).

We applied GPS to a series of evolutionary models of masses $1 M_{\odot}$ and $1.5 M_{\odot}$ on the red-giant branch. The comparison of the values of $\Delta\Pi_{1,g}$ with the respective asymptotic values from these models are shown in Figs. 5 and 6. We tested the effect of both the total number of available

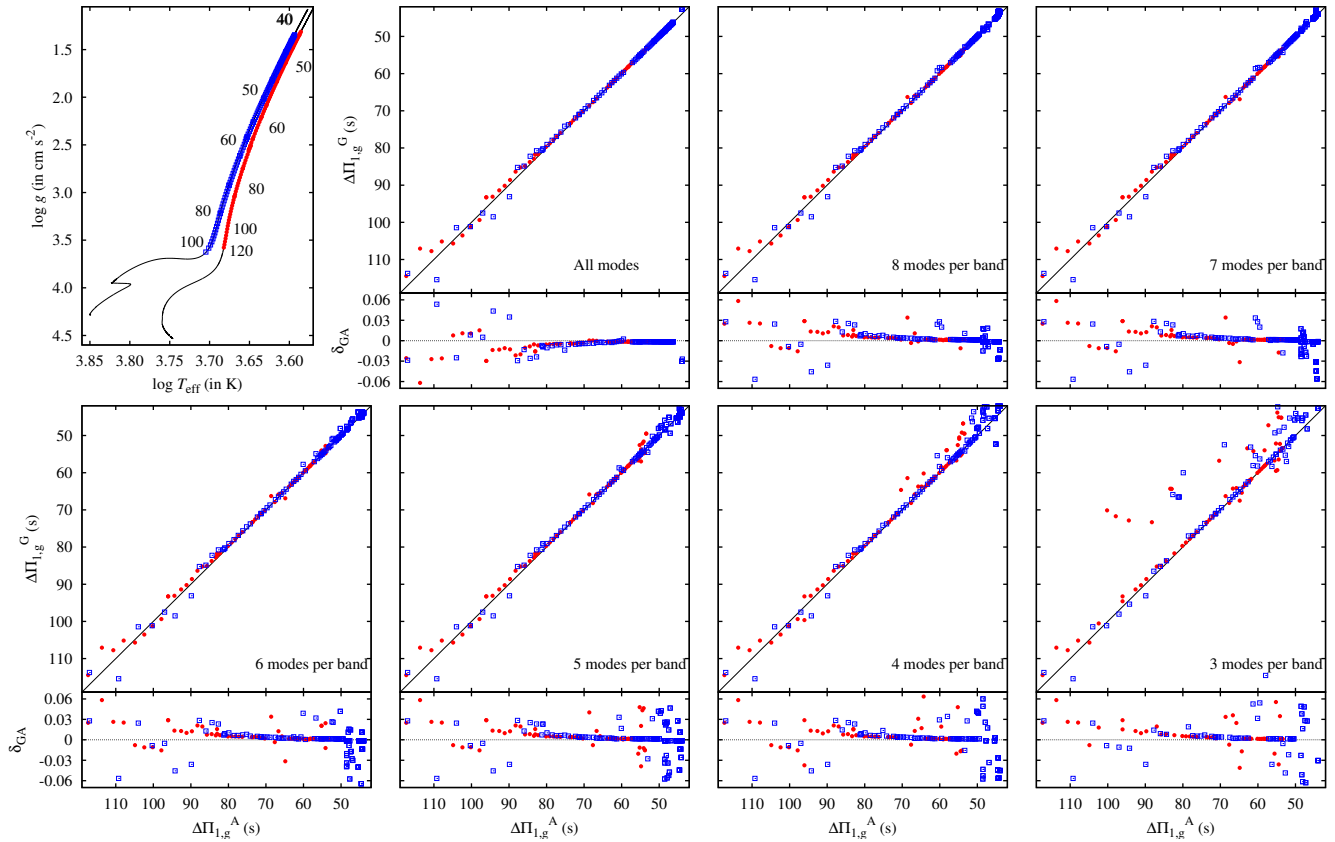


Figure 5. Comparison of $\Delta\Pi_{1,g}$ values obtained with GPS for models with the corresponding asymptotic values are shown for different choices of number of modes in each band. The top left panel shows the tested models of $1 M_{\odot}$ (red filled circles) and $1.5 M_{\odot}$ (blue empty squares) in a $\log T_{\text{eff}}\text{--}\log g$ diagram. The asymptotic values of $\Delta\Pi_{1,g}$ (in s) from the models are indicated alongside the evolutionary tracks (black continuous curves). In the upper part of each of the other panels the $\Delta\Pi_{1,g}$ values obtained from GPS ($\Delta\Pi_{1,g}^G$) are plotted against the asymptotic values ($\Delta\Pi_{1,g}^A$). In the lower part the fractional differences between the two, $\delta_{GA} \equiv 1 - \Delta\Pi_{1,g}^G / \Delta\Pi_{1,g}^A$, are shown.

bands and the number of modes available in each band on the results produced by GPS.

In the first test we used 5 bands around the frequency of maximum oscillation power, ν_{max} , computed by the scaling relation of Kjeldsen & Bedding (1995) from the model, but varied the number of $l = 1$ modes in each band from 3 to 8. These modes were the ones with lowest inertia values in each band. We also tested GPS using all the available modes in 5 bands. The results of the comparison of the values obtained from GPS with the asymptotic values from the models are shown in Fig. 5. In general, the $\Delta\Pi_{1,g}$ values obtained by GPS agree very closely with the asymptotic values. Although the difference between the two increases as the number of modes in each band are decreased, for at least 5 modes per band, the $\Delta\Pi_{1,g}$ value found by GPS is within 5% of the asymptotic value for almost all the models that we considered. Even with only 4 or 3 modes per band, GPS can find the correct value within this limit for models with $\Delta\Pi_{1,g}$ values between 50 and 110 s.

In the second test we used only five $l = 1$ modes with the lowest inertia values in each band but varied the total number of bands from 2 to 7. As expected, the $\Delta\Pi_{1,g}$ values are determined with higher accuracy when using a larger number of bands. The comparison of these results with the corresponding asymptotic values of $\Delta\Pi_{1,g}$ are shown in Fig. 6.

Again, the values from GPS agree with the asymptotic values to within 5% for nearly all cases with at least 4 bands. Using only 2 or 3 bands we can still get values within this limit for models with $\Delta\Pi_{1,g}$ greater than 60 s.

In general, we find that GPS can be reliably applied only to frequencies of models with $\log g$ values between 3.6 and 1.3 (see top left panel of Fig. 5). We recommend that GPS should be applied to observed RGB stars only within such limits of $\log g$.

3.2 Application of GPS on observed frequencies

For the observed frequencies, the number of modes available is much less compared to models. Specifically, the g-dominated modes which constitute the central ridge of the vertical pattern are absent and only the p-dominated modes are present in the observed spectrum. However, provided that a few mixed dipole modes are present in the spectrum, GPS can successfully determine $\Delta\Pi_{1,g}$. Of course, the uncertainty of the estimated value reduces with the number of modes that are detected close to the vertical ridge. We elaborate on the uncertainties in more detail in Section 3.3. To illustrate the application of GPS to real stellar data, we show here the results of three red-giant stars, KIC 10200377, KIC 9145955, and KIC 5866737, observed by

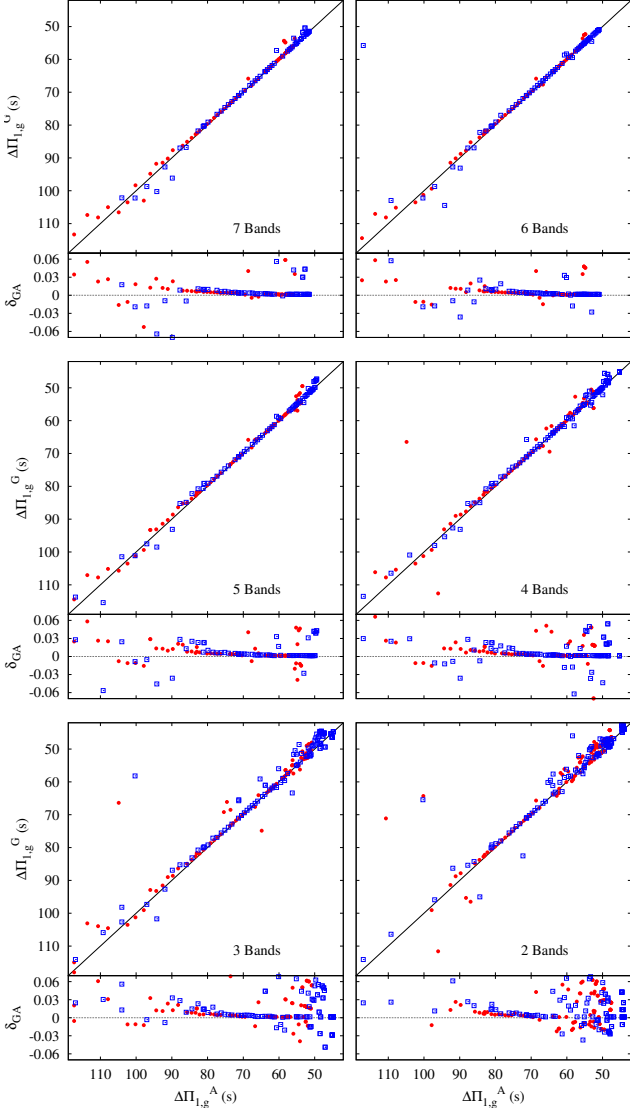


Figure 6. Comparison of $\Delta\Pi_{1,g}$ values obtained with GPS for models with the corresponding asymptotic values are shown for different choices of total number of bands. The symbols have the same meaning as in Fig. 5.

the *Kepler* space mission (Borucki et al. 2008; Gilliland et al. 2010) during its nominal operation. The position of these stars are shown on the HR diagram in Fig. 7.

The photometric timeseries were gathered during the first 12 quarters of the *Kepler* mission, where quarter 0 lasted for only 10 days, quarter 1 lasted for 30 days and all other quarters for nominally 90 days. This provided us with time-series data of over a 1000 days length. We used observations with a 29.4-minute sampling. For more details about *Kepler* data and their treatment, we refer to e.g. Jenkins et al. (2010); García et al. (2011).

Fig. 8 shows the period echelle diagrams for these three red giants: KIC 10200377 with $\Delta\Pi_{1,g} = 81.59$ s, KIC 9145955 with $\Delta\Pi_{1,g} = 76.98$ s, and KIC 5866737 with $\Delta\Pi_{1,g} = 68.51$ s, respectively. In this figure, it can be seen from the left panels that most of the $l = 1$ modes in the observed spectrum have low values of period spacing and thus

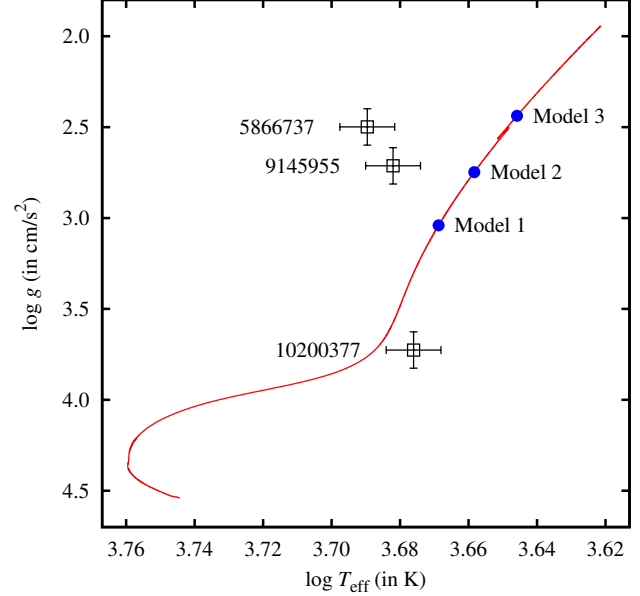


Figure 7. The position of three red-giant stars observed by *Kepler* are shown on the $\log T_{\text{eff}} - \log g$ diagram. The effective temperatures are taken from the *Kepler* Input Catalogue (KIC) for KIC 5866737 and from the APOGEE catalogue for the other two stars. The $\log g$ values are from KIC. Also shown, by the red line, is the evolutionary track of a $1M_{\odot}$ model. The blue dots indicate the three models that we discuss in this paper.

are the p-dominated modes. The g-dominated modes which have higher and uniform value of period spacing as seen in Fig. 2(a) are absent in the observed spectrum. Nevertheless, GPS is able to identify a value of $\Delta\Pi_{1,g}$ which produces the expected vertical alignment of the dipole modes in the period echelle diagram, as seen in the right panels of Fig. 8. A few of the observed modes have period spacing of nearly double the average value, which indicates that a neighbouring dipole mode has not been detected. Thus GPS can also help in flagging these missed modes in the power spectrum.

3.3 Estimation of the Uncertainties in $\Delta\Pi_{1,g}$

So far, we have described the application of GPS to either model frequencies or to observed frequencies without regard to their associated uncertainties. In observed data the uncertainties in the frequency values will affect the determination of $\Delta\Pi_{1,g}$ through GPS. Also it is important to know the maximum permissible uncertainty in observed frequencies for which GPS can be applied reliably.

The effects of the uncertainties in the frequencies are considered by repeating the procedure carried out by GPS for 10000 realisations of the data, produced by perturbation of the frequencies by random values corresponding to a normal distribution with standard deviation equal to the given 1σ uncertainty in the frequencies. This approach is justified by the fact that only the frequencies of $l = 1$ modes which are narrow due to the high inertia are perturbed.

It is conceivable that for low values of the assumed uncertainty in the frequencies GPS would return values of

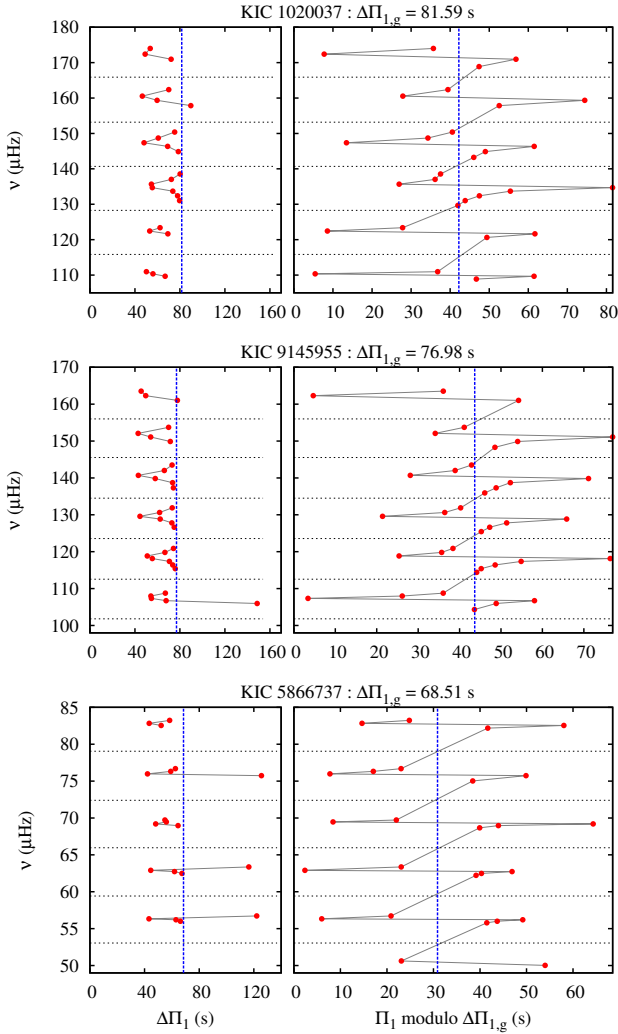


Figure 8. Results obtained with GPS for three red giants with *Kepler* frequencies: KIC 10200377 (top) KIC 9145955 (middle), and KIC 5866737 (bottom). The left panel in each plots the frequencies as a function of observed $\Delta\Pi_1$, while the right panel shows the period echelle diagram. The symbols and the lines have the same meaning as in Fig. 2. The value of $\Delta\Pi_{1,g}$ determined by GPS is indicated at the top of each pair of panels. In the left panels of the latter two stars the large values of $\Delta\Pi_1$ for a few modes indicate that a neighbouring $l = 1$ mode has not been detected.

$\Delta\Pi_{1,g}$ which are close to the actual value for a majority of the realisations. In the Monte Carlo exercise, this would be reflected in a single peak in the histogram of the $\Delta\Pi_{1,g}$ values centred around the actual value. The median value of $\Delta\Pi_{1,g}$ for all the realisations would be the estimated value and the width of this peak, measured in terms of 34% area coverage on either side of the median value, would be a fair representation of the uncertainty in $\Delta\Pi_{1,g}$.

As the uncertainty in the frequencies increases, however, other values of $\Delta\Pi_{1,g}$ become likely and we get distinct multiple peaks in the histogram at discrete values away from the correct value of $\Delta\Pi_{1,g}$. In such cases, the overall median and the uncertainty based on 34% area coverage on either side of that value would not be a true representation of the situation. Instead, we have chosen to report the three most

probable values and associated uncertainties along with respective probabilities. Graphically, these would be the three most significant peaks in the histogram with highest area coverage. Specifically, we define the peaks in the histogram as follows. The bin with the highest population is chosen along with its neighbouring bins till the value in a bin drops to below 10% of the maximum value. These bins together constitute the most significant peak. From among the remaining bins the one with the next highest value is chosen and the same criterion is applied to include its neighbouring bins. These bins together form the second highest peak, and so on. For each peak we provide the median value under that peak, its 1σ uncertainty measured in the way described above, and the probability, p , of that value, which is the fractional area under that peak.

This exercise was carried out with three red-giant models as well as the above-mentioned three observed red giants. The models are chosen such that they lie at different positions on the red giant branch and are labelled as Model 1, Model 2 and Model 3, respectively, in increasing order of their luminosities. All the models lie on the same evolutionary track of a $1 M_\odot$ star with solar-like chemical abundances (see Fig. 7).

Since for models the entire theoretically computed frequency spectrum is available, we test GPS for a variety of cases with varying selection of frequencies and the associated uncertainties. The selection of frequencies was carried out in two ways. First, we have considered three different ranges of frequencies corresponding to 4, 5 and 6 times the large separation, each centred around ν_{\max} , i.e., we chose the range of frequencies to be $\nu_{\max} \pm k\Delta\nu$, for $k = 2.0, 2.5, 3.0$. Second, we applied different cutoffs on the mode inertia to select a different number of g -dominated modes in the spectrum. Typically, we have created four sets: one with all the dipole modes (without any restriction on mode inertia), one with only three or four most p -dominated modes in each band (corresponding to an inertia cutoff close to the minima), and two others with intermediate numbers of dipole modes. Since the observed amplitude of dipole modes are related to the mode inertia (Dupret et al. 2009), selection based on the inertia would mimic the observed spectra with varying detection limits based on mode amplitudes.

This selection is illustrated in Fig. 9 for Model 2 for a case with 5 radial orders. The results for the four different choices of the mode set, in decreasing order of inertia cutoffs are shown by the histograms in the figure. When the full set of modes is used, there is only one dominant peak in the histogram, very close to the actual value of $\Delta\Pi_{1,g}$ (middle left panel of Fig. 9). This is because the presence of the g -dominated modes forming the vertical ridge in the period echelle diagram have a large influence in constraining the $\Delta\Pi_{1,g}$. However, for the same reason, in some realisations, when a few of these crucial frequencies are perturbed significantly from their true values, they influence the estimate of $\Delta\Pi_{1,g}$ strongly and alternative values of $\Delta\Pi_{1,g}$ are found. These appear as smaller peaks in the histogram. When an inertia cutoff is applied so that the most g -dominated modes are omitted, the estimation of $\Delta\Pi_{1,g}$ becomes less stable and a secondary peak at a lower value is found, although the median value still lies very close to the actual value. However, on further lowering the inertia cutoff, the value of $\Delta\Pi_{1,g}$ actually stabilises again. This is because the vertical ridge

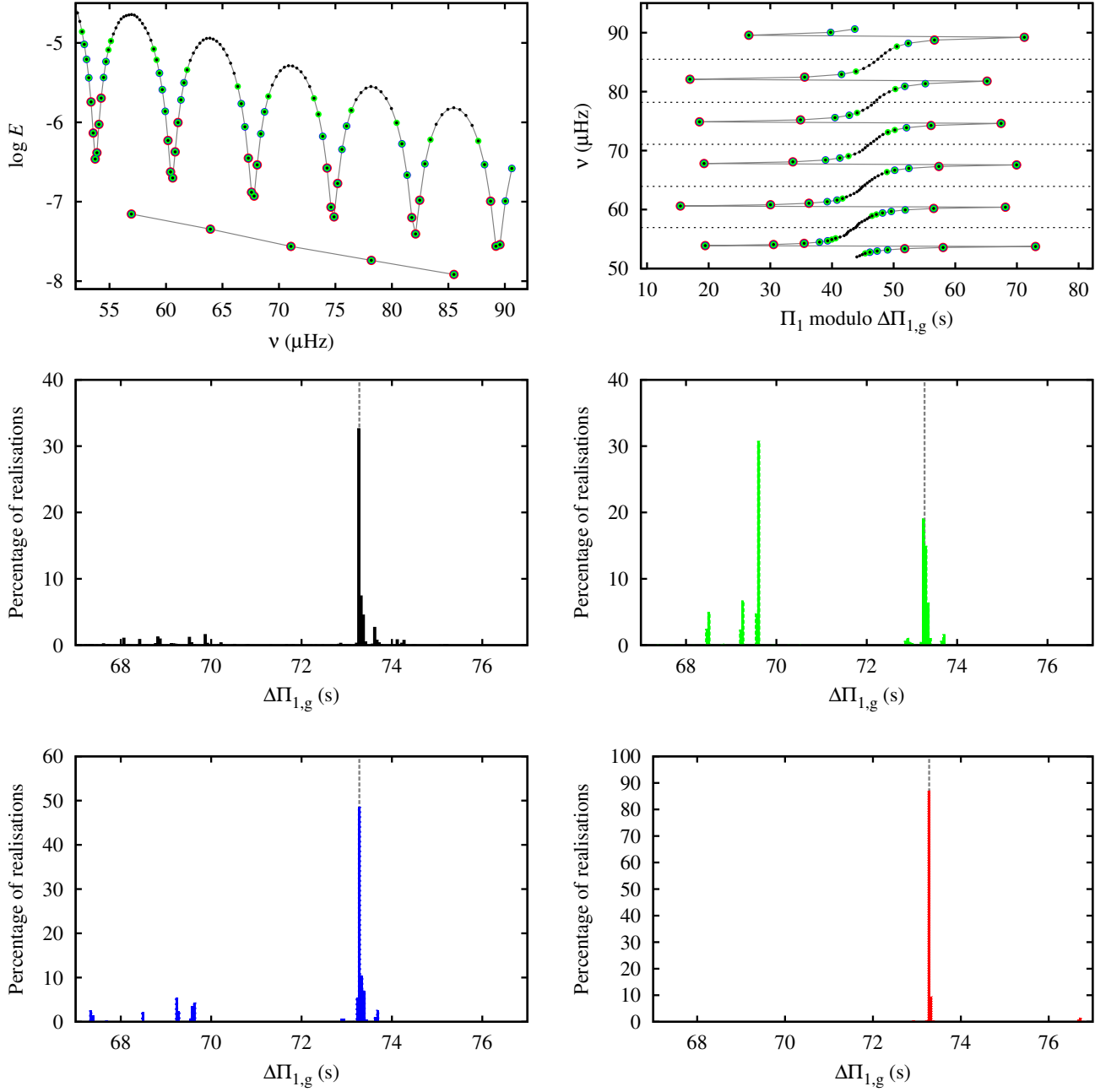


Figure 9. Results of the Monte Carlo exercise with the frequencies of Model 2 with a uniform uncertainty of $0.01\mu\text{Hz}$. The top left panel shows the inertia of the $l=0$ and $l=1$ modes of the model. The four different choices of the mode sets used for the MC exercise are shown in different colours, while green, blue and red circles denote sets with progressively lower cutoffs applied on the mode inertia. The top right panel shows the period echelle diagram where $\Delta\Pi_{1,g}$ has been set to the value of 73.28s found from the unperturbed model frequencies. The symbols and lines are similar to that of Fig. 2 with the different colours corresponding to the four sets as depicted in the top left panel. The remaining four panels show the histograms of the $\Delta\Pi_{1,g}$ values found in the MC exercise for the four sets, again corresponding to the same colours as depicted in the top left panel. In each of the bottom four panels the vertical dotted line shows the value of $\Delta\Pi_{1,g}$ obtained for the unperturbed model frequencies.

is now mainly determined by the two dipole modes closest to the radial mode in each order and the condition for symmetric distribution of the p-dominated modes becomes more important to find $\Delta\Pi_{1,g}$.

For each of these artificially created samples of modes containing radial and dipole modes we have considered four to six different values for the uncertainty in the frequencies. Throughout this exercise, we have considered uniform uncertainties in all the mode frequencies. Thus for each of the three models, we have carried out the Monte Carlo exercise for nearly 60 different data sets.

The uncertainties in $\Delta\Pi_{1,g}$ for different levels of uncertainties in frequencies for the three models and the three observed *Kepler* red giants are given in Tables A1–A4. As an illustration of the exercise, in Fig. 10 we show the histograms for the $\Delta\Pi_{1,g}$ values found by GPS for different datasets constructed from the theoretical frequencies of Model 2, as described above.

For each of the mode sets described above for the three models, we applied GPS after perturbing the frequencies with random uncertainties corresponding to normal distributions with widths of 0.001, 0.005, 0.010, 0.050 and 0.100 μHz . The results for the three models show similar trends for uncertainty in $\Delta\Pi_{1,g}$. For the full set of frequencies the large number of g-dominated modes ensures that $\Delta\Pi_{1,g}$ is estimated to be very close to the asymptotic value for small frequency uncertainties. For the smallest frequency uncertainty of 0.001 μHz , typically almost all the realisations produce a unique value of $\Delta\Pi_{1,g}$. However, as the uncertainty in frequencies increases, the probability of obtaining the correct value of $\Delta\Pi_{1,g}$ decreases, which is manifested in the appearance of multiple peaks in the histogram of $\Delta\Pi_{1,g}$ values. For the cases where we choose fewer number of modes, namely, only those with lower inertia, the probability of obtaining a value close to the correct value decreases with decreasing number of modes, before again increasing for the cases with the least number of modes. A closer inspection of the situation reveals that the apparent decrease of the probability of the correct value being obtained is due to appearance of a few values very close to the correct one but different by more than one bin in the histogram. If one would choose a larger binwidth of the histogram of $\Delta\Pi_{1,g}$, one would regain the correct value with a larger uncertainty, although not all values within the range quoted by the 1σ uncertainties would be actually permissible. Finally, the increase in probability of finding the correct value of $\Delta\Pi_{1,g}$ with fewer modes is essentially due to the comparatively larger effect of the p-dominated modes in constraining $\Delta\Pi_{1,g}$ through the symmetrical distribution criterion, as compared to the determination of the vertical ridge from the g-dominated modes. However, if the number of modes per band falls below three, the determination of $\Delta\Pi_{1,g}$ becomes unreliable even at small frequency uncertainties (see Tables A1–A3).

Although the trend of the uncertainties in $\Delta\Pi_{1,g}$ with increasing frequency uncertainties is broadly similar in the three models, there are clear differences in the details. In general, the most stable determination of $\Delta\Pi_{1,g}$ happens for Model 1, which is the youngest among the three models. For this model, the density of g-modes is least, and one can reliably estimate $\Delta\Pi_{1,g}$ even at frequency uncertainties up to 0.100 μHz in several cases. For Model 2, $\Delta\Pi_{1,g}$ is correctly estimated up to frequency uncertainties of 0.050 μHz , while

for Model 3 GPS fails to find a reliable value of $\Delta\Pi_{1,g}$ even at frequency uncertainties of 0.010 μHz in some cases. The reason behind this behaviour can be understood in the following way. The coupling between the modes trapped in the envelope and those in the core decreases as the star evolves up the red-giant branch. This implies that the number of dipole modes with low inertia decreases with age (Dupret et al. 2009).

For the method used by GPS, a stronger coupling is beneficial for the determination of $\Delta\Pi_{1,g}$. In case of stronger coupling the transition from p-dominated modes in one band to p-dominated modes in the next band through the g-dominated dipole modes around the location of a radial mode is less steep, i.e. the g-dominated modes cover a larger range of inertia. In GPS the determination of $\Delta\Pi_{1,g}$ depends crucially on the mixed dipole modes closest to the radial mode at the boundary of a band through the weighing factors in Eq. (6). In more evolved models with weaker coupling (e.g., Model 3), small perturbations in the dipole frequencies closest to the radial modes have large impact on the determination of $\Delta\Pi_{1,g}$ thanks to the steep slope originating from the weak coupling. On the other hand, when fewer modes are chosen based on mode inertia the dipole modes closest to the radial modes are separated by too large a frequency interval, again providing difficulties for GPS to determine $\Delta\Pi_{1,g}$ reliably. In cases with stronger coupling (e.g., Model 1) the less steep transition of the p-dominated regions reduces the influence of small perturbations in the dipole frequencies, thus providing a more robust determination of $\Delta\Pi_{1,g}$. In this case, GPS works even for relatively higher frequency uncertainties.

In the cases of the three observed *Kepler* stars we examine the results of the Monte Carlo exercise with up to five times the nominal 1σ uncertainty in the frequencies ($= 0.022 \mu\text{Hz}$) determined from the peakbagging exercise. These results are shown in Table A4. We find that for KIC 10200377 even when the uncertainty in the frequencies is increased up to 5σ , we obtain values consistent with $\Delta\Pi_{1,g} = 81.54^{+0.06}_{-0.04}$ s, as found with the 1σ uncertainties, albeit with decreasing probabilities. This is consistent with the trend shown by Model 1, which has a very similar $\Delta\Pi_{1,g}$ value as this star. For the star KIC 9145955 which is located higher in the red-giant branch, the results remain consistent up to 2σ uncertainties in frequencies. In this case, a secondary peak at 77.72 s, which is only 0.7 s seconds away from the highest peak, is found even at small frequency perturbations. In the case of the further evolved star KIC 5866737, GPS is unable to determine $\Delta\Pi_{1,g}$ at all when the frequency uncertainties are beyond 3σ . The last two cases are similar in behaviour to Models 2 and 3, respectively.

In general, we find that when the sum of the probabilities of the three highest peaks in the histogram is less than around 75%, the value of $\Delta\Pi_{1,g}$ determined by GPS is not very reliable. In such cases, we essentially have a number of closely spaced distinct values of $\Delta\Pi_{1,g}$ which have comparable probabilities. In many cases it might be possible to quote a median value of $\Delta\Pi_{1,g}$ if we use a larger binwidth, leading to a larger uncertainty value.

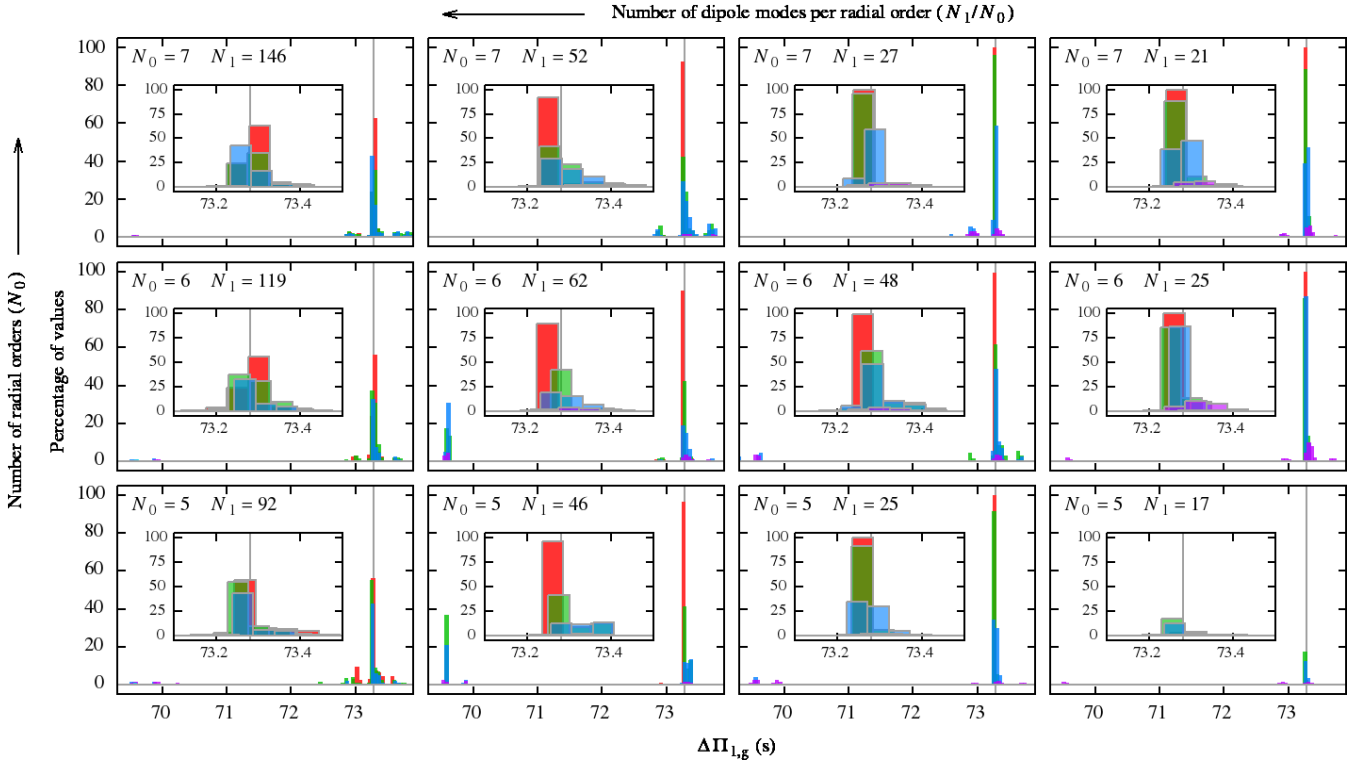


Figure 10. Results of the Monte Carlo exercise with different uncertainties assumed for the frequencies of a $1M_{\odot}$ model (Model 2) are shown. In each panel the histograms of the distribution of $\Delta\Pi_{1,g}$ determined by GPS are shown for assumed uncertainties of $0.001 \mu\text{Hz}$ (in red), $0.005 \mu\text{Hz}$ (in green), $0.010 \mu\text{Hz}$ (in blue), $0.050 \mu\text{Hz}$ (in magenta) and $0.100 \mu\text{Hz}$ (in cyan). The different panels show the different data sets considered for the exercise in terms of number of radial orders (N_0) and number of dipole modes (N_1). The grey vertical line shows the $\Delta\Pi_{1,g}$ obtained with the full set of unperturbed frequencies of the model. The insets in each panel show the main peaks of the histograms. Numerical estimates of $\Delta\Pi_{1,g}$ from this exercise are given in Table A2.

3.4 Iteration between peakbagging and GPS

Peakbagging is the craft of finding, identifying and fitting oscillation modes in a Fourier power spectrum of an oscillating star. To find real oscillation signal, statistical tests are often applied (e.g. Hekker et al. 2010; Appourchaux 2014, and references therein). These statistical tests essentially provide a probability of a feature being due to noise or signal. Depending on the threshold used, this implies that a fraction of the features selected to be signal can actually be due to noise, and the other way around; features that are actual signal are not selected. Missing information is often less harmful than wrong information and hence making sure that all signal features are indeed due to genuine stellar oscillations has priority. However, a larger number of observed oscillation modes could provide additional information and constraints, required to draw inferences.

When the oscillation signals have been detected, they need to be identified in terms of radial order, spherical degree and azimuthal order. Methods such as the universal pattern (Mosser et al. 2011, 2012a) are developed for this purpose. Additionally, for solar-like oscillations accurate frequencies, mode widths and heights with uncertainties can be obtained from Lorentzian fits to the oscillation signals in the Fourier power spectrum. This information is of importance when using the oscillation modes to compute intrinsic stellar properties and infer the internal stellar structure of a star. For GPS the frequencies and mode degree are the most im-

portant observational inputs to compute the period spacing. We note here that GPS can, in principle, work for any azimuthal order (m) as long as the azimuthal order is the same for all modes. Here it is, however, always applied to modes with $m = 0$.

In case GPS cannot constrain the period spacing it is possible to identify features in the Fourier power spectrum that do not conform to the expectations. For these features visual checks are performed in the Fourier power spectrum to gauge whether the feature is a genuine oscillation mode, its identification is correct (in this way we can for instance identify a mode with a different azimuthal order) and/or if the frequency is accurately determined. In this way it is possible to iterate between peakbagging and GPS to make sure that correctly identified true signals are used for the determination of the period spacing.

An example of this iteration process is shown in Fig. 11 where both the Fourier power spectrum of KIC 9145955 and the corresponding period echelle diagrams are shown. The blue and red dots in the Fourier power spectrum (top panel of Fig. 11) indicate the initially detected $l = 1$ modes. These frequencies did not provide a proper period echelle diagram (bottom left panel of Fig. 11). Using the information of the problematic frequencies and the computed approximate period spacing we have been able to optimise the detection and identification of the $l = 1$ modes. In this way we discarded incorrectly identified features of the power spectrum and identified more modes over a wider frequency range (red dots

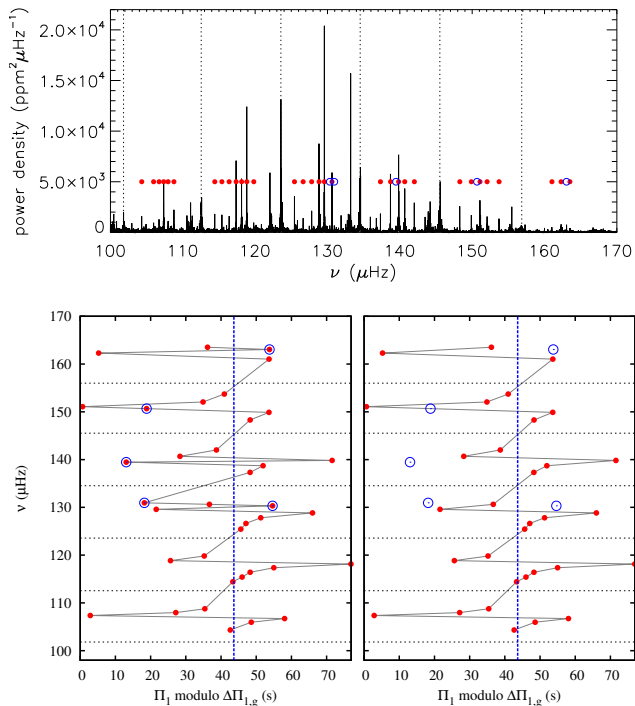


Figure 11. The iterative process of using GPS to improve mode detection and identification is illustrated for the *Kepler* red-giant star KIC 9145955. The top panel shows the power spectrum where the radial modes are indicated by dotted vertical lines and the dipole modes are marked by red dots. The dipole modes which were deemed to have been misidentified based on input from GPS are encircled in blue. The bottom two panels show the period echelle diagrams, where the lines and symbols have the same meaning as in Fig. 2. In the bottom left panel is the diagram using all the initially identified modes, with the suspected misidentifications encircled in blue. The bottom right panel shows the period echelle diagram where the misidentified modes (empty blue circles) have been excluded from the analysis.

in top panel and right bottom panel of Fig. 11), which allowed GPS to determine the period spacing of KIC 9145955 to be 76.98 ± 0.03 s.

4 CONCLUSION

We have devised a new method (GPS, g-mode period spacing finder) to estimate the period spacing of g-modes in red-giant stars. Such modes can usually not be detected in the observed Fourier spectrum of a red giant because of their low amplitudes. However, the period spacing of these modes is related to the conditions in the core, specifically, the buoyancy frequency. Therefore, if one is able to determine the g-mode period spacing from the observed modes, it may be used as a strong constraint in finding a suitable model for a star.

The automated method devised here is based on the period echelle diagram and essentially seeks the period spacing for which a vertical alignment of the gravity-dominated modes is present as well as a symmetric distribution of the pressure-dominated modes. The method has been extensively tested on model frequencies. For each model different

sets of frequencies have been selected based on their inertia, different frequency ranges have been taken and different (uniform) uncertainties on the frequencies have been tested in a Monte Carlo approach. This shows that often more than one period spacing provides a possible answer. These period spacing values are distinct with ranges without possible solutions separating them. Therefore, we provide the three most probable period spacings for each investigated case (both models and observations) with their probability and uncertainty. For both the models and observations we obtain period spacings with high probability when the uncertainties on the frequencies are in the range $0.01\text{--}0.05\text{ }\mu\text{Hz}$ or below. In case of the models these are indeed consistent with the asymptotic period spacings.

Although, GPS is only applied to red-giant branch models and stars in this work, it has already been applied successfully to a red-clump star by Silva Aguirre et al. (2014). The potential of GPS for red-clump stars will be explored more extensively elsewhere.

Finally, GPS has significant potential once the extraction of mixed modes of large numbers of stars is possible. First attempts for this are already present such as the work by Stello et al. (2013) and Mosser et al. (2012a). However, determinations of accurate individual frequencies for a large number of stars are currently not available and hence such analysis is beyond the scope of this paper. Work to develop tools to get these accurate individual frequencies is underway and application of GPS to such a large sample will be published in forthcoming publications.

5 ACKNOWLEDGMENTS

AD, AM and UG acknowledge support from the National Initiative on Undergraduate Science (NIUS) programme of HBCSE (TIFR). SH acknowledges financial support from the Netherlands Organisation for Scientific Research (NWO). The research leading to the presented results has received funding from the European Research Council under the European Community's Seventh Framework Programme (FP7/2007-2013) / ERC grant agreement no 338251 (StellarAges).

REFERENCES

- Aerts, C., Christensen-Dalsgaard, J., & Kurtz, D. W. 2010, *Asteroseismology*, Astronomy and Astrophysics Library, ISBN 978-1-4020-5178-4, Springer 2010
- Aizenman, M., Smeyers, P., & Weigert, A. 1977, *A&A*, 58, 41
- Angulo, C., Arnould, M., Rayet, M., et al. 1999, *Nuclear Physics A*, 656, 3
- Appourchaux, T. 2014, *Asteroseismology*, 22nd Canary Islands Winter School of Astrophysics., p.123, 123
- Beck, P. G., Bedding, T. R., Mosser, B., et al. 2011, *Science*, 332, 205
- Beck, P. G., Montalbán, J., Kallinger, T., et al. 2012, *Nature*, 481, 55
- Bedding, T. R., Mosser, B., Huber, D., et al. 2011, *Nature*, 471, 608

Bedding, T. R. 2014, *Asteroseismology*, 22nd Canary Islands Winter School of Astrophysics., p.60, 60

Borucki, W., Koch, D., Basri, G., et al. 2008, *IAU Symposium*, 249, 17

Cantiello, M., Mankovich, C., Bildsten, L., Christensen-Dalsgaard, J., & Paxton, B. 2014, arXiv:1405.1419

Ceillier, T., Eggenberger, P., García, R. A., & Mathis, S. 2013, *A&A*, 555, A54

Chaplin, W. J. & Miglio, A. 2013, *ARA&A*, 51, 353

Christensen-Dalsgaard, J. 2011, arXiv:1106.5946

Christensen-Dalsgaard, J. 2008, *Ap&SS*, 316, 113

Cox, J., & Giuli, R. 1968, *Principles of Stellar Structure: Physical principles*, *Principles of Stellar Structure No. v. 1* (Gordon and Breach)

Deheuvels, S., García, R. A., Chaplin, W. J., et al. 2012, *ApJ*, 756, 19

Deheuvels, S., Doğan, G., Goupil, M. J., et al. 2014, *A&A*, 564, A27

Dupret M.-A., et al. 2009, *A&A*, 506, 57

Ferguson, J. W., Alexander, D. R., Allard, F., et al. 2005, *ApJ*, 623, 585

García, R. A., Hekker, S., Stello, D., et al. 2011, *MNRAS*, 414, L6

Gilliland, R. L., Brown, T. M., Christensen-Dalsgaard, J., et al. 2010, *PASP*, 122, 131

Goupil, M. J., Mosser, B., Marques, J. P., et al. 2013, *A&A*, 549, A75

Goupil, M., Deheuvels, S., Marques, J., et al. 2014, *IAU Symposium*, 301, 161

Grevesse, N., & Sauval, A. J. 1998, *Space Sci. Rev.*, 85, 161

Hekker S. 2013, *AdSpR*, 52, 1581

Hekker, S., Barban, C., Baudin, F., et al. 2010, *A&A*, 520, A60

Hekker, S. & Mazumdar, A. 2013, *Precision Asteroseismology*, *Proceedings IAU Symposium No. 301*, 2014

Iglesias, C. A., & Rogers, F. J. 1996, *ApJ*, 464, 943

Imbriani, G., Costantini, H., Formicola, A., et al. 2005, *European Physical Journal A*, 25, 455

Jenkins, J. M., Caldwell, D. A., Chandrasekaran, H., et al. 2010, *ApJ*, 713, L120

Kjeldsen, H., & Bedding, T. R. 1995, *A&A*, 293, 87

Krishna Swamy, K. S. 1966, *ApJ*, 145, 174

Kunz, R., Fey, M., Jaeger, M., et al. 2002, *ApJ*, 567, 643

Marques, J. P., Goupil, M. J., Lebreton, Y., et al. 2013, *A&A*, 549, A74

Montalbán, J., Miglio, A., Noels, A., Scuflaire, R., & Ventura, P. 2010, *ApJ*, 721, L182

Mosser B., et al. 2011, *A&A*, 525, L9

Mosser, B., Goupil, M. J., Belkacem, K., et al. 2012, *A&A*, 540, A143

Mosser, B., Goupil, M. J., Belkacem, K., et al. 2012, *A&A*, 548, A10

Mosser B., et al. 2014, arXiv:1411.1082

Ouazzani, R.-M., Goupil, M. J., Dupret, M.-A., & Marques, J. P. 2013, *A&A*, 554, A80

Paxton, B., Bildsten, L., Dotte, A., et al. 2011, *ApJS*, 192, 3

Rogers, F. J., & Nayfonov, A. 2002, *ApJ*, 576, 1064

Shibahashi, H. 1979, *PASJ*, 31, 87

Silva Aguirre, V., Ruchti, G. R., Hekker, S., et al. 2014, *ApJ*, 784, L16

Stello, D., Huber, D., Bedding, T. R., et al. 2013, *ApJ*, 765,

L41 ‘

Unno, W., Osaki, Y., Ando, H., Saio, H., & Shibahashi, H. 1989, *Nonradial oscillations of stars*, Tokyo: University of Tokyo Press, 1989, 2nd ed.

APPENDIX A: DETAILED RESULTS OF MONTE CARLO EXERCISE

Table A1. Results of a Monte Carlo exercise with a $1M_{\odot}$ red giant model at an age of 12.4 Gyr (Model 1). N_0 and N_1 are the number of $l = 0$ and $l = 1$ modes, respectively, that are used in the exercise. $\delta\nu$ is the uncertainty introduced in the frequencies and p is the probability of the associated $\Delta\Pi_{1,g}$ value. The asymptotic value of $\Delta\Pi_{1,g}$ for this model is 82.61 s.

N_0	N_1	$\delta\nu$ (μHz)									
(Range in μHz)		0.001		0.005		0.010		0.050		0.100	
		p	$\Delta\Pi_{1,g}$ (s)	p	$\Delta\Pi_{1,g}$ (s)	p	$\Delta\Pi_{1,g}$ (s)	p	$\Delta\Pi_{1,g}$ (s)	p	$\Delta\Pi_{1,g}$ (s)
6 (75.00)	60	1.0000	$82.48^{+0.01}_{-0.01}$	0.8263	$82.49^{+0.02}_{-0.02}$	0.5762	$82.50^{+0.15}_{-0.03}$	0.1546	$84.82^{+0.08}_{-0.06}$	0.1778	$85.97^{+0.33}_{-0.26}$
		0.1008	$82.62^{+0.13}_{-0.08}$	0.2785	$83.34^{+0.07}_{-0.03}$	0.1379	$83.45^{+0.07}_{-0.07}$	0.1127	$87.11^{+0.08}_{-0.08}$
		0.0404	$83.34^{+0.02}_{-0.02}$	0.0932	$81.70^{+0.05}_{-0.20}$	0.1208	$87.11^{+0.04}_{-0.03}$	0.0794	$83.53^{+0.11}_{-0.11}$
	32	1.0000	$82.48^{+0.01}_{-0.01}$	1.0000	$82.47^{+0.01}_{-0.01}$	0.9974	$82.47^{+0.03}_{-0.02}$	0.6605	$82.50^{+0.03}_{-0.04}$	0.4337	$82.50^{+0.09}_{-0.07}$
		0.0019	$82.62^{+0.05}_{-0.04}$	0.1717	$83.33^{+0.10}_{-0.07}$	0.2104	$83.42^{+0.10}_{-0.13}$
		0.0003	$81.51^{+0.02}_{-0.02}$	0.0736	$81.56^{+0.17}_{-0.09}$	0.1167	$84.64^{+0.21}_{-0.17}$
	20	1.0000	$81.71^{+0.01}_{-0.01}$	0.9899	$81.70^{+0.02}_{-0.02}$	0.8760	$81.73^{+0.03}_{-0.04}$	0.4986	$82.51^{+0.03}_{-0.04}$	0.4880	$82.51^{+0.05}_{-0.04}$
		0.0095	$82.50^{+0.02}_{-0.03}$	0.1240	$82.50^{+0.02}_{-0.02}$	0.4345	$81.73^{+0.04}_{-0.03}$	0.2798	$81.72^{+0.08}_{-0.11}$
		0.0003	$82.55^{+0.02}_{-0.02}$	0.0129	$68.98^{+0.02}_{-0.02}$	0.0353	$68.96^{+0.04}_{-0.04}$
	17	1.0000	$81.71^{+0.01}_{-0.01}$	0.9999	$81.71^{+0.02}_{-0.02}$	0.9899	$81.70^{+0.03}_{-0.02}$	0.8062	$81.74^{+0.05}_{-0.03}$	0.5690	$81.76^{+0.06}_{-0.06}$
		0.0001	$81.76^{+0.02}_{-0.02}$	0.0101	$81.80^{+0.02}_{-0.02}$	0.1782	$82.54^{+0.04}_{-0.03}$	0.3188	$82.54^{+0.05}_{-0.05}$
		0.0092	$81.88^{+0.02}_{-0.02}$	0.0362	$71.24^{+0.07}_{-0.08}$
6 (62.50)	48	1.0000	$82.48^{+0.01}_{-0.01}$	0.8573	$82.49^{+0.03}_{-0.04}$	0.5375	$82.50^{+0.15}_{-0.04}$	0.3078	$87.24^{+0.03}_{-0.03}$	0.1401	$87.19^{+0.21}_{-0.15}$
		0.0820	$82.63^{+0.08}_{-0.07}$	0.2217	$83.16^{+0.02}_{-0.02}$	0.1224	$83.59^{+0.05}_{-0.06}$	0.1352	$85.73^{+0.22}_{-0.12}$
		0.0479	$83.16^{+0.02}_{-0.02}$	0.1741	$83.34^{+0.16}_{-0.03}$	0.1214	$88.15^{+0.05}_{-0.03}$	0.0854	$88.15^{+0.12}_{-0.06}$
	24	1.0000	$81.71^{+0.01}_{-0.01}$	0.9650	$81.74^{+0.02}_{-0.02}$	0.8157	$81.73^{+0.02}_{-0.02}$	0.3833	$82.50^{+0.04}_{-0.04}$	0.2573	$82.53^{+0.12}_{-0.07}$
		0.0300	$81.69^{+0.02}_{-0.02}$	0.1005	$72.74^{+0.03}_{-0.02}$	0.2788	$81.73^{+0.14}_{-0.05}$	0.1292	$83.46^{+0.10}_{-0.10}$
		0.0039	$72.74^{+0.02}_{-0.02}$	0.0265	$81.68^{+0.02}_{-0.02}$	0.0946	$83.45^{+0.09}_{-0.05}$	0.1211	$72.70^{+0.07}_{-0.08}$
	18	0.9987	$82.47^{+0.02}_{-0.02}$	0.6545	$82.46^{+0.02}_{-0.02}$	0.5449	$82.48^{+0.02}_{-0.02}$	0.4711	$82.48^{+0.04}_{-0.03}$	0.3255	$82.48^{+0.07}_{-0.08}$
		0.0013	$81.72^{+0.02}_{-0.02}$	0.2696	$81.71^{+0.02}_{-0.02}$	0.3281	$81.73^{+0.02}_{-0.02}$	0.1890	$72.71^{+0.06}_{-0.06}$	0.1425	$72.69^{+0.07}_{-0.07}$
		0.0557	$72.72^{+0.02}_{-0.02}$	0.1204	$72.73^{+0.02}_{-0.02}$	0.1821	$81.72^{+0.04}_{-0.03}$	0.0898	$71.91^{+0.08}_{-0.06}$
	13	1.0000	$81.71^{+0.01}_{-0.01}$	0.9994	$81.73^{+0.02}_{-0.04}$	0.9468	$81.72^{+0.02}_{-0.02}$	0.5291	$81.70^{+0.05}_{-0.07}$	0.3462	$81.70^{+0.09}_{-0.12}$
		0.0006	$71.24^{+0.02}_{-0.02}$	0.0379	$71.23^{+0.04}_{-0.02}$	0.1957	$71.26^{+0.02}_{-0.02}$	0.1449	$71.27^{+0.04}_{-0.04}$
		0.0151	$81.67^{+0.02}_{-0.02}$	0.1352	$61.97^{+0.04}_{-0.02}$	0.1117	$61.97^{+0.04}_{-0.03}$
4 (50.23)	39	0.9995	$81.71^{+0.02}_{-0.02}$	0.5776	$82.49^{+0.03}_{-0.04}$	0.6377	$82.49^{+0.05}_{-0.02}$	0.1418	$83.49^{+0.21}_{-0.15}$	0.0950	$86.86^{+0.16}_{-0.22}$
		0.0005	$82.46^{+0.02}_{-0.02}$	0.4008	$81.71^{+0.02}_{-0.02}$	0.1251	$83.19^{+0.02}_{-0.02}$	0.1314	$85.84^{+0.25}_{-0.06}$	0.0700	$79.24^{+0.41}_{-0.26}$
		0.0176	$82.62^{+0.12}_{-0.07}$	0.1011	$81.73^{+0.02}_{-0.03}$	0.1035	$84.37^{+0.08}_{-0.07}$	0.0331	$77.49^{+0.05}_{-0.05}$
	26	1.0000	$81.71^{+0.01}_{-0.01}$	0.9997	$81.72^{+0.02}_{-0.02}$	0.9296	$81.73^{+0.02}_{-0.04}$	0.4497	$82.50^{+0.11}_{-0.04}$	0.2048	$82.50^{+0.15}_{-0.19}$
		0.0002	$73.32^{+0.02}_{-0.02}$	0.0436	$82.49^{+0.02}_{-0.02}$	0.1565	$83.45^{+0.07}_{-0.05}$	0.1943	$83.43^{+0.11}_{-0.13}$
		0.0001	$82.47^{+0.02}_{-0.02}$	0.0149	$73.33^{+0.02}_{-0.03}$	0.0941	$84.35^{+0.05}_{-0.05}$	0.1210	$84.37^{+0.08}_{-0.07}$
	22	1.0000	$81.71^{+0.01}_{-0.01}$	1.0000	$81.71^{+0.01}_{-0.01}$	1.0000	$81.71^{+0.04}_{-0.03}$	0.4267	$81.72^{+0.03}_{-0.04}$	0.3023	$82.52^{+0.08}_{-0.06}$
		0.3280	$82.49^{+0.04}_{-0.03}$	0.1248	$83.45^{+0.10}_{-0.11}$
		0.0321	$56.75^{+0.08}_{-0.03}$	0.1160	$81.72^{+0.11}_{-0.15}$
	14	1.0000	$81.71^{+0.01}_{-0.01}$	0.9999	$81.73^{+0.03}_{-0.04}$	0.9529	$81.72^{+0.03}_{-0.04}$	0.2830	$81.73^{+0.04}_{-0.03}$	0.1321	$82.49^{+0.05}_{-0.04}$
		0.0001	$71.24^{+0.02}_{-0.02}$	0.0253	$71.24^{+0.02}_{-0.02}$	0.1409	$66.12^{+0.02}_{-0.03}$	0.1072	$66.10^{+0.04}_{-0.05}$
		0.0156	$81.89^{+0.02}_{-0.02}$	0.1089	$61.98^{+0.02}_{-0.02}$	0.0861	$61.97^{+0.04}_{-0.03}$

Table A2. Results of a Monte Carlo exercise with a $1M_{\odot}$ red giant model at an age of 12.5 Gyr (Model 2). The quantities shown have the same meaning as in Table A1. The asymptotic value of $\Delta\Pi_{1,g}$ for this model is 73.49 s.

N_0	N_1	$\delta\nu$ (μHz)									
(Range		0.001		0.005		0.010		0.050		0.100	
in μHz)		p	$\Delta\Pi_{1,g}$ (s)	p	$\Delta\Pi_{1,g}$ (s)	p	$\Delta\Pi_{1,g}$ (s)	p	$\Delta\Pi_{1,g}$ (s)	p	$\Delta\Pi_{1,g}$ (s)
7 (46.19)	146	0.9074	$73.30^{+0.02}_{-0.04}$	0.6699	$73.29^{+0.03}_{-0.04}$	0.6449	$73.27^{+0.05}_{-0.03}$	0.0688	$78.72^{+0.06}_{-0.06}$	0.2578	$66.23^{+1.44}_{-1.83}$
		0.0256	$72.90^{+0.02}_{-0.02}$	0.0937	$72.92^{+0.10}_{-0.05}$	0.1122	$73.76^{+0.09}_{-0.13}$	0.0603	$78.20^{+0.06}_{-0.06}$	0.0307	$68.43^{+0.07}_{-0.07}$
		0.0218	$73.40^{+0.02}_{-0.02}$	0.0417	$74.16^{+0.08}_{-0.03}$	0.0338	$74.37^{+0.08}_{-0.02}$	0.0371	$68.84^{+0.03}_{-0.04}$	0.0302	$68.84^{+0.06}_{-0.07}$
	52	0.9263	$73.25^{+0.02}_{-0.02}$	0.7389	$73.27^{+0.05}_{-0.03}$	0.6214	$73.29^{+0.06}_{-0.04}$	0.1104	$85.35^{+0.04}_{-0.05}$	0.0319	$85.37^{+0.07}_{-0.09}$
		0.0583	$73.33^{+0.07}_{-0.04}$	0.1364	$73.69^{+0.03}_{-0.06}$	0.1657	$73.69^{+0.07}_{-0.04}$	0.0541	$68.81^{+0.05}_{-0.05}$	0.0251	$84.78^{+0.08}_{-0.07}$
		0.0130	$72.94^{+0.02}_{-0.05}$	0.0967	$72.90^{+0.03}_{-0.04}$	0.0672	$72.86^{+0.04}_{-0.03}$	0.0527	$69.19^{+0.04}_{-0.05}$	0.0218	$85.95^{+0.08}_{-0.06}$
	27	1.0000	$73.26^{+0.01}_{-0.01}$	0.9590	$73.26^{+0.02}_{-0.02}$	0.6772	$73.29^{+0.02}_{-0.02}$	0.1087	$73.32^{+0.06}_{-0.04}$	0.5955	$55.33^{+5.43}_{-3.94}$
		0.0176	$72.91^{+0.02}_{-0.02}$	0.1148	$72.92^{+0.04}_{-0.04}$	0.1014	$72.93^{+0.06}_{-0.06}$	0.0222	$68.89^{+0.33}_{-0.10}$
		0.0100	$73.34^{+0.06}_{-0.04}$	0.0512	$77.04^{+0.03}_{-0.02}$	0.0719	$77.55^{+0.06}_{-0.06}$	0.0184	$73.34^{+0.06}_{-0.06}$
	21	1.0000	$73.26^{+0.01}_{-0.01}$	0.9973	$73.26^{+0.02}_{-0.02}$	0.8618	$73.28^{+0.03}_{-0.04}$	0.1412	$73.32^{+0.04}_{-0.05}$	0.0237	$85.06^{+0.09}_{-0.08}$
		0.0023	$76.00^{+0.02}_{-0.03}$	0.0649	$76.00^{+0.02}_{-0.02}$	0.0562	$85.11^{+0.06}_{-0.06}$	0.0214	$78.51^{+0.07}_{-0.07}$
		0.0003	$65.76^{+0.02}_{-0.02}$	0.0215	$73.35^{+0.02}_{-0.02}$	0.0445	$72.93^{+0.05}_{-0.05}$	0.0187	$73.33^{+0.06}_{-0.06}$
5 (38.65)	119	0.8834	$73.29^{+0.03}_{-0.04}$	0.7940	$73.28^{+0.04}_{-0.04}$	0.4460	$73.28^{+0.05}_{-0.02}$	0.0502	$77.77^{+0.07}_{-0.07}$	0.0271	$69.20^{+0.05}_{-0.06}$
		0.0686	$72.98^{+0.04}_{-0.05}$	0.0681	$73.00^{+0.04}_{-0.13}$	0.0341	$59.97^{+0.02}_{-0.02}$	0.0486	$68.83^{+0.03}_{-0.04}$	0.0226	$68.84^{+0.05}_{-0.05}$
		0.0303	$73.40^{+0.02}_{-0.02}$	0.0589	$73.66^{+0.06}_{-0.05}$	0.0332	$62.72^{+0.02}_{-0.02}$	0.0340	$68.05^{+0.04}_{-0.03}$	0.0195	$69.58^{+0.05}_{-0.05}$
	62	0.8994	$73.25^{+0.02}_{-0.02}$	0.4248	$73.28^{+0.02}_{-0.02}$	0.4136	$73.29^{+0.05}_{-0.04}$	0.0973	$68.81^{+0.04}_{-0.03}$	0.2813	$73.87^{+2.57}_{-3.03}$
		0.0721	$73.33^{+0.07}_{-0.04}$	0.3100	$69.60^{+0.04}_{-0.03}$	0.3547	$69.60^{+0.02}_{-0.02}$	0.0779	$69.21^{+0.04}_{-0.05}$	0.1250	$79.83^{+1.37}_{-1.40}$
		0.0251	$72.89^{+0.05}_{-0.05}$	0.0830	$69.23^{+0.02}_{-0.02}$	0.0898	$69.25^{+0.02}_{-0.04}$	0.0765	$69.58^{+0.03}_{-0.04}$	0.0242	$77.79^{+0.08}_{-0.08}$
	48	0.9968	$73.26^{+0.02}_{-0.02}$	0.7863	$73.29^{+0.04}_{-0.02}$	0.7139	$73.29^{+0.05}_{-0.03}$	0.0909	$73.32^{+0.05}_{-0.05}$	0.0305	$84.79^{+0.08}_{-0.08}$
		0.0032	$73.36^{+0.05}_{-0.05}$	0.0839	$73.64^{+0.04}_{-0.03}$	0.0846	$69.61^{+0.03}_{-0.04}$	0.0709	$69.57^{+0.04}_{-0.03}$	0.0296	$85.37^{+0.09}_{-0.08}$
		0.0613	$72.89^{+0.03}_{-0.02}$	0.0784	$69.24^{+0.04}_{-0.02}$	0.0682	$68.80^{+0.04}_{-0.03}$	0.0256	$83.05^{+0.07}_{-0.07}$
	25	1.0000	$73.26^{+0.01}_{-0.01}$	0.9972	$73.26^{+0.02}_{-0.02}$	0.9640	$73.28^{+0.02}_{-0.02}$	0.2482	$73.32^{+0.05}_{-0.05}$	0.0268	$69.28^{+0.31}_{-0.11}$
		0.0027	$76.71^{+0.03}_{-0.02}$	0.0224	$76.71^{+0.03}_{-0.04}$	0.0506	$68.81^{+0.04}_{-0.04}$	0.0180	$73.34^{+0.07}_{-0.07}$
		0.0001	$73.35^{+0.02}_{-0.02}$	0.0034	$73.22^{+0.02}_{-0.02}$	0.0342	$76.71^{+0.03}_{-0.04}$	0.0131	$68.80^{+0.08}_{-0.06}$
5 (30.76)	92	0.7762	$73.28^{+0.06}_{-0.02}$	0.7104	$73.26^{+0.04}_{-0.02}$	0.5375	$73.27^{+0.04}_{-0.02}$	0.0445	$77.76^{+0.07}_{-0.06}$	0.0494	$68.67^{+0.19}_{-0.26}$
		0.1465	$73.02^{+0.03}_{-0.03}$	0.1069	$72.93^{+0.06}_{-0.10}$	0.0546	$62.71^{+0.02}_{-0.02}$	0.0400	$68.83^{+0.04}_{-0.04}$	0.0266	$69.20^{+0.06}_{-0.07}$
		0.0635	$73.58^{+0.06}_{-0.02}$	0.0549	$73.64^{+0.09}_{-0.04}$	0.0437	$54.89^{+0.03}_{-0.04}$	0.0326	$69.91^{+0.03}_{-0.04}$	0.0233	$69.56^{+0.06}_{-0.06}$
	46	0.9668	$73.26^{+0.02}_{-0.02}$	0.6239	$73.29^{+0.07}_{-0.03}$	0.3787	$73.33^{+0.05}_{-0.06}$	0.0488	$69.54^{+0.04}_{-0.03}$	0.8130	$57.41^{+6.63}_{-5.12}$
		0.0174	$73.33^{+0.04}_{-0.03}$	0.3674	$69.58^{+0.02}_{-0.02}$	0.2182	$69.58^{+0.02}_{-0.02}$	0.0408	$73.32^{+0.05}_{-0.05}$	0.0323	$70.35^{+0.71}_{-0.45}$
		0.0145	$72.91^{+0.02}_{-0.02}$	0.0028	$63.68^{+0.02}_{-0.02}$	0.0485	$54.73^{+0.02}_{-0.02}$	0.0320	$69.88^{+0.03}_{-0.03}$	0.0309	$69.18^{+0.34}_{-0.35}$
	25	1.0000	$73.26^{+0.01}_{-0.01}$	0.9731	$73.26^{+0.02}_{-0.02}$	0.6901	$73.27^{+0.04}_{-0.03}$	0.0689	$69.54^{+0.05}_{-0.05}$	0.4665	$58.07^{+5.20}_{-5.43}$
		0.0078	$69.55^{+0.02}_{-0.04}$	0.0970	$67.35^{+0.02}_{-0.02}$	0.0525	$73.32^{+0.05}_{-0.06}$	0.3484	$71.98^{+5.52}_{-4.34}$
		0.0034	$72.86^{+0.02}_{-0.02}$	0.0463	$65.50^{+0.02}_{-0.02}$	0.0520	$69.89^{+0.05}_{-0.04}$	0.0090	$82.59^{+0.11}_{-0.09}$
	17	0.9565	$77.13^{+0.02}_{-0.02}$	0.4966	$77.14^{+0.03}_{-0.04}$	0.3841	$77.15^{+0.05}_{-0.05}$	0.0563	$77.13^{+0.06}_{-0.06}$	0.0202	$93.53^{+0.08}_{-0.10}$
		0.0230	$73.28^{+0.02}_{-0.02}$	0.2832	$64.14^{+0.02}_{-0.04}$	0.3224	$64.13^{+0.04}_{-0.03}$	0.0506	$77.53^{+0.08}_{-0.06}$	0.0180	$94.19^{+0.10}_{-0.10}$
		0.0129	$64.12^{+0.02}_{-0.02}$	0.1760	$73.26^{+0.02}_{-0.02}$	0.1585	$73.27^{+0.03}_{-0.02}$	0.0485	$73.32^{+0.07}_{-0.06}$	0.0164	$99.77^{+0.11}_{-0.09}$

Table A3. Results of a Monte Carlo exercise with a $1M_{\odot}$ red giant model at an age of 12.6 Gyr (Model 3). The quantities shown have the same meaning as in Table A1. The asymptotic value of $\Delta\Pi_{1,g}$ for this model is 62.15 s.

N_0 (Range in μHz)	N_1	$\delta\nu$ (μHz)							
		0.001		0.005		0.010		0.050	
		p	$\Delta\Pi_{1,g}$ (s)	p	$\Delta\Pi_{1,g}$ (s)	p	$\Delta\Pi_{1,g}$ (s)	p	$\Delta\Pi_{1,g}$ (s)
6 (27.36)	422	0.8710	$62.05^{+0.02}_{-0.02}$	0.0676	$62.07^{+0.02}_{-0.02}$	0.0393	$53.55^{+0.02}_{-0.02}$	0.8152	$55.48^{+10.7}_{-7.24}$
		0.0795	$62.14^{+0.03}_{-0.04}$	0.0272	$55.87^{+0.02}_{-0.02}$	0.0270	$52.51^{+0.05}_{-0.02}$	0.0914	$78.28^{+3.51}_{-2.74}$
		0.0309	$62.37^{+0.08}_{-0.03}$	0.0237	$52.52^{+0.02}_{-0.02}$	0.0129	$50.95^{+0.02}_{-0.02}$	0.0062	$86.74^{+0.27}_{-0.25}$
	146	0.8552	$62.06^{+0.02}_{-0.02}$	0.2898	$62.06^{+0.03}_{-0.04}$	0.0956	$62.07^{+0.12}_{-0.04}$	0.9390	$63.23^{+7.51}_{-6.49}$
		0.0663	$62.15^{+0.03}_{-0.04}$	0.1372	$60.58^{+0.02}_{-0.02}$	0.0919	$60.44^{+0.03}_{-0.04}$	0.0222	$79.71^{+1.01}_{-0.89}$
		0.0471	$60.46^{+0.02}_{-0.02}$	0.0949	$62.18^{+0.02}_{-0.02}$	0.0859	$60.61^{+0.14}_{-0.04}$	0.0085	$50.46^{+0.32}_{-0.29}$
	81	0.7484	$62.08^{+0.02}_{-0.02}$	0.1624	$62.06^{+0.02}_{-0.02}$	0.0579	$60.58^{+0.03}_{-0.02}$	0.8786	$74.87^{+10.7}_{-10.2}$
		0.0917	$62.19^{+0.04}_{-0.02}$	0.1291	$67.37^{+0.02}_{-0.02}$	0.0543	$62.06^{+0.02}_{-0.04}$	0.0387	$94.17^{+0.84}_{-0.76}$
		0.0847	$60.58^{+0.02}_{-0.02}$	0.0698	$58.27^{+0.02}_{-0.02}$	0.0516	$58.27^{+0.02}_{-0.02}$	0.0136	$96.01^{+0.20}_{-0.29}$
	28	0.9119	$62.06^{+0.02}_{-0.02}$	0.4170	$62.07^{+0.03}_{-0.04}$	0.1485	$62.06^{+0.03}_{-0.04}$	0.8200	$61.16^{+11.8}_{-8.33}$
		0.0426	$59.46^{+0.02}_{-0.02}$	0.0865	$55.23^{+0.02}_{-0.02}$	0.0465	$55.22^{+0.08}_{-0.03}$	0.0923	$84.60^{+3.02}_{-2.54}$
		0.0103	$57.46^{+0.02}_{-0.02}$	0.0601	$59.47^{+0.02}_{-0.03}$	0.0318	$66.36^{+0.02}_{-0.02}$	0.0063	$94.59^{+0.25}_{-0.23}$
6 (22.78)	333	0.8775	$62.07^{+0.02}_{-0.03}$	0.1510	$62.06^{+0.02}_{-0.02}$	0.3745	$58.78^{+0.78}_{-0.91}$	0.8689	$62.62^{+4.22}_{-3.53}$
		0.0883	$62.20^{+0.14}_{-0.07}$	0.0554	$63.50^{+0.02}_{-0.02}$	0.0409	$60.26^{+0.04}_{-0.15}$	0.0621	$72.12^{+2.02}_{-1.24}$
		0.0228	$62.53^{+0.02}_{-0.02}$	0.0515	$60.61^{+0.02}_{-0.02}$	0.0238	$60.44^{+0.03}_{-0.02}$	0.0492	$55.82^{+0.57}_{-0.85}$
	35	0.7534	$62.07^{+0.02}_{-0.02}$	0.2041	$62.08^{+0.10}_{-0.04}$	0.0434	$70.91^{+0.02}_{-0.02}$	0.8626	$59.10^{+10.7}_{-6.85}$
		0.0803	$62.17^{+0.02}_{-0.02}$	0.1047	$60.72^{+0.03}_{-0.12}$	0.0406	$76.59^{+0.03}_{-0.04}$	0.0386	$80.33^{+1.34}_{-1.02}$
		0.0798	$60.72^{+0.02}_{-0.02}$	0.0649	$65.70^{+0.03}_{-0.02}$	0.0304	$72.50^{+0.02}_{-0.02}$	0.0209	$86.18^{+0.91}_{-0.93}$
	22	0.7403	$62.07^{+0.02}_{-0.02}$	0.1675	$62.07^{+0.02}_{-0.03}$	0.0715	$62.08^{+0.10}_{-0.06}$	0.7925	$59.14^{+10.9}_{-7.06}$
		0.0954	$67.47^{+0.02}_{-0.02}$	0.0836	$59.46^{+0.03}_{-0.11}$	0.0566	$57.52^{+0.06}_{-0.10}$	0.1309	$82.59^{+4.10}_{-3.75}$
		0.0413	$57.42^{+0.02}_{-0.02}$	0.0674	$55.22^{+0.02}_{-0.02}$	0.0443	$55.22^{+0.02}_{-0.08}$	0.0143	$93.05^{+0.59}_{-0.51}$
	11	0.9340	$57.47^{+0.02}_{-0.02}$	0.2283	$57.45^{+0.02}_{-0.02}$	0.0470	$57.44^{+0.04}_{-0.03}$	0.7396	$57.55^{+9.60}_{-5.91}$
		0.0649	$64.87^{+0.02}_{-0.02}$	0.1457	$64.88^{+0.03}_{-0.04}$	0.0421	$64.88^{+0.02}_{-0.02}$	0.1427	$78.61^{+4.08}_{-3.51}$
		0.0009	$59.87^{+0.02}_{-0.02}$	0.0529	$62.05^{+0.02}_{-0.02}$	0.0380	$63.13^{+0.02}_{-0.02}$	0.0356	$86.64^{+1.27}_{-1.32}$
4 (18.20)	257	0.8109	$62.07^{+0.02}_{-0.02}$	0.1354	$62.05^{+0.02}_{-0.02}$	0.4164	$56.40^{+1.06}_{-1.23}$	0.9079	$67.07^{+6.38}_{-6.02}$
		0.0346	$60.60^{+0.03}_{-0.04}$	0.0658	$59.40^{+0.02}_{-0.02}$	0.2561	$58.78^{+0.60}_{-0.64}$	0.0504	$80.75^{+1.70}_{-1.12}$
		0.0244	$60.87^{+0.02}_{-0.02}$	0.0428	$60.60^{+0.02}_{-0.02}$	0.0682	$54.00^{+0.37}_{-0.35}$	0.0122	$54.09^{+0.46}_{-0.52}$
	51	0.4769	$62.08^{+0.02}_{-0.02}$	0.2376	$62.05^{+0.02}_{-0.02}$	0.1018	$62.11^{+0.15}_{-0.09}$	0.9063	$60.93^{+9.78}_{-7.55}$
		0.3750	$59.34^{+0.03}_{-0.02}$	0.1386	$59.46^{+0.03}_{-0.02}$	0.0907	$60.71^{+0.13}_{-0.14}$	0.0517	$81.76^{+2.29}_{-1.75}$
		0.1101	$60.86^{+0.03}_{-0.04}$	0.1089	$76.50^{+0.02}_{-0.02}$	0.0730	$59.21^{+0.13}_{-0.15}$	0.0027	$85.54^{+0.14}_{-0.19}$
	30	0.9354	$62.05^{+0.05}_{-0.03}$	0.1869	$62.06^{+0.02}_{-0.04}$	0.0457	$57.44^{+0.12}_{-0.44}$	0.8192	$60.03^{+11.4}_{-7.57}$
		0.0212	$60.80^{+0.08}_{-0.08}$	0.0737	$62.17^{+0.02}_{-0.02}$	0.0305	$76.58^{+0.03}_{-0.04}$	0.1112	$83.84^{+3.80}_{-3.06}$
		0.0053	$60.59^{+0.02}_{-0.02}$	0.0634	$63.57^{+0.02}_{-0.02}$	0.0172	$74.80^{+0.02}_{-0.02}$	0.0156	$90.54^{+0.59}_{-0.82}$
	19	0.7021	$67.46^{+0.02}_{-0.02}$	0.2500	$62.07^{+0.02}_{-0.02}$	0.0896	$62.07^{+0.10}_{-0.03}$	0.6682	$54.27^{+6.09}_{-3.36}$
		0.2775	$62.06^{+0.02}_{-0.02}$	0.1272	$67.46^{+0.02}_{-0.02}$	0.0549	$55.21^{+0.07}_{-0.08}$	0.2381	$71.14^{+6.32}_{-4.77}$
		0.0060	$67.51^{+0.02}_{-0.02}$	0.0795	$55.22^{+0.02}_{-0.02}$	0.0355	$67.46^{+0.02}_{-0.02}$	0.0185	$84.83^{+0.86}_{-0.71}$

Table A4. Results of the Monte Carlo exercises with three red-giant stars observed by the *Kepler* satellite. The quantities shown have the same meaning as in Table A1.

KIC id	$\delta\nu (\sigma = 0.022\mu\text{Hz})$									
	1σ		2σ		3σ		4σ		5σ	
	p	$\Delta\Pi_{1,g} \text{ (s)}$	p	$\Delta\Pi_{1,g} \text{ (s)}$	p	$\Delta\Pi_{1,g} \text{ (s)}$	p	$\Delta\Pi_{1,g} \text{ (s)}$	p	$\Delta\Pi_{1,g} \text{ (s)}$
10200377	0.8087	$81.54^{+0.06}_{-0.04}$	0.6339	$81.53^{+0.06}_{-0.05}$	0.5506	$81.52^{+0.06}_{-0.05}$	0.4370	$81.52^{+0.07}_{-0.06}$	0.3122	$81.53^{+0.08}_{-0.07}$
	0.1169	$82.51^{+0.02}_{-0.02}$	0.1993	$82.52^{+0.03}_{-0.04}$	0.1757	$82.51^{+0.06}_{-0.08}$	0.1976	$84.84^{+0.05}_{-0.04}$	0.2658	$84.86^{+0.06}_{-0.05}$
	0.0190	$81.69^{+0.04}_{-0.03}$	0.0558	$83.42^{+0.02}_{-0.03}$	0.1006	$84.83^{+0.04}_{-0.03}$	0.1303	$82.49^{+0.08}_{-0.11}$	0.0889	$82.47^{+0.09}_{-0.10}$
9145955	0.5389	$76.98^{+0.04}_{-0.02}$	0.3463	$76.99^{+0.09}_{-0.04}$	0.2796	$79.81^{+0.07}_{-0.17}$	0.2495	$79.77^{+0.10}_{-0.15}$	0.2206	$81.91^{+0.08}_{-0.11}$
	0.3022	$77.72^{+0.03}_{-0.04}$	0.3262	$77.72^{+0.06}_{-0.05}$	0.1745	$77.72^{+0.07}_{-0.06}$	0.2033	$81.92^{+0.07}_{-0.09}$	0.1929	$79.74^{+0.13}_{-0.13}$
	0.0708	$76.42^{+0.02}_{-0.03}$	0.1434	$79.85^{+0.03}_{-0.06}$	0.1645	$77.00^{+0.09}_{-0.06}$	0.1759	$78.87^{+0.22}_{-0.12}$	0.1307	$78.91^{+0.17}_{-0.19}$
5866737	0.4902	$68.49^{+0.04}_{-0.05}$	0.0803	$68.48^{+0.06}_{-0.05}$	0.4771	$38.37^{+8.24}_{-5.99}$
	0.0807	$72.59^{+0.04}_{-0.03}$	0.0371	$72.61^{+0.06}_{-0.05}$	0.0165	$68.48^{+0.06}_{-0.05}$
	0.0564	$68.76^{+0.03}_{-0.03}$	0.0298	$68.78^{+0.07}_{-0.05}$	0.0087	$64.79^{+0.05}_{-0.05}$